

NEAR-FIELD IMAGING VIA INVERSE SCATTERING

By

Junshan Lin

A DISSERTATION

Submitted to  
Michigan State University  
in partial fulfillment of the requirements  
for the degree of

DOCTOR OF PHILOSOPHY

Applied Mathematics

2011

## ABSTRACT

### NEAR-FIELD IMAGING VIA INVERSE SCATTERING

By

**Junshan Lin**

Near-field optics is an emerging research topic in the past few decades, mostly motivated by applications in the near-field microscopy in an effort to break the diffraction limit. In the far-field imaging, only the propagating wave components with spatial frequency below the wavenumber are available, and it is well-known that the resolution of the image is approximately  $\lambda/2$  (diffraction limit) [17, 51, 53]. In the near field, however, the bandwidth of the spatial frequency may be expanded by taking account of the evanescent (exponentially decayed) waves. Nowadays there exist various configurations for the near-field microscopies, see for example [51]. However, it is recognized that the images obtained from the near-field microscopies are problematic by visualizing the object in an analogical way [18, 47]. Therefore, the inverse scattering theory is applied to understand how the structure of the scattering object is encoded in the measured scattered field. When single scattering (or Born approximation) is assumed, the studies are complete for the near-field scanning optical microscopy (NSOM) and the total internal reflection microscopy (TIRT) within the framework of the inverse scattering theory [19, 20, 57].

In this thesis, we focus on one specific problem where the imaging target is a ground plane with some local disturbance. The data is collected in the near-field regime with a distance above the surface displacement that is smaller than the wavelength. In the recent paper [29], a linearized model has been introduced for the nonlinear inverse scattering problem by the single scattering assumption. The authors also proposed a broadband imaging strategy for denoising and improving the resolution of the image. In the thesis, we investigate the more general case by considering the full scattering model, for which the linearized model in [29] is no longer

valid. By the analysis of the scattered field, it is confirmed that the evanescent wave modes which are not accessible in the far-field regime become significant in the near field. Evanescent wave modes make it possible to break the diffraction limit. It is shown that such exponentially decayed modes of the scattered wave contain the high spatial frequency information (fine features) of the profile. We formulate explicitly the connection between the evanescent wave modes and the high frequency components of the surface displacement, and present a new numerical scheme to reconstruct the surface displacement from the boundary measurements. By extracting the information carried by the evanescent modes effectively, it is shown that the resolution of the reconstructed image is significantly improved in the near field. Numerical examples show that images with a resolution of  $\lambda/10$  are obtained.

To overcome the ill-posedness and the presence of local minima associated with this nonlinear imaging problem, we propose to use multiple frequency data to image the profile of the surface displacement in the second part of the thesis. The main idea is to march from the lowest wavenumber to the highest wavenumber. At the fixed wavenumber, by an analysis of the domain derivative for the forward scattering map, a vector field is chosen such that the defined cost functional decreases. The reconstructed profile evolves with the chosen vector field at the fixed wavenumber and the evolution process continues until it reaches the highest wavenumber. The proposed reconstructed scheme is able to capture the main feature of the profile at low frequency and recover the fine details at higher frequency. In particular, for a multiple scale profile, it resolves the fine scale with sufficiently high frequency.

## ACKNOWLEDGMENT

I am deeply grateful to my thesis advisor Professor Gang Bao, whose continuous support and encouragements were invaluable for my four-year PhD studies at Michigan State University. He introduced to me the project on near-field imaging, and generously shared his wide expertise with me. His view on applied mathematics also helps me to shape my own understanding in the field, and will continue to influence me in the long run. I am also much obliged to him for helping me to improve my English writing skill, and for providing opportunities of attending conferences where I met the leading figures in the field and did presentations.

I would like to thank Professors Zhengfang Zhou, Andrew Christlieb, Chichia Chiu, Di Liu and Jianliang Qian for serving in my thesis committee. I am so indebted to them and Professor Habib Ammari for providing letters of reference. I am also grateful to Professor Baisheng Yan and Barbara Miller for taking care of everything, in particular for their help during my first year study as a fresh PhD student.

Many thanks also go to the research group here at Michigan State University. We have various interesting discussions and a lot of fun together. Thanks all the group members for sharing your expertise and happiness with me: Justin Droba, Guanghui Hu, Jun Lai, Peijun Li, Songting Luo, Yuanchang Sun, Yuliang Wang, Zhengfu Xu, KiHyun Yun, and Hai Zhang. Thanks in particular Yuanchang, Yuliang and Maureen for taking care of me when I first came to US in 2007. Thanks all my friends here, in particular Lianzhang Bao, Langhua Hu, Jie Niu, Xun Wang, Tianshuang Wu and Qiong Zheng.

Finally, I would like to thank my parents and parents in law for their strong support. I owe my deepest gratitude to my wife Yu Chen for all the sacrifice she made. I can always feel her strong support behind me!

# TABLE OF CONTENTS

	List of Figures . . . . .	vii
<b>1</b>	<b>Introduction . . . . .</b>	<b>1</b>
1.1	Near-field Optics . . . . .	1
1.2	Near-field Imaging Microscopy . . . . .	3
1.3	Near-field Imaging via Inverse Scattering . . . . .	4
<b>2</b>	<b>Mathematical Theory of Inverse Problem . . . . .</b>	<b>7</b>
2.1	Concepts of Ill-Posed Problem . . . . .	7
2.2	Singular Value Decomposition for Linear Compact Operators . . . . .	8
2.3	Regularization Methods for Linear Problems . . . . .	10
2.4	Regularization Methods for Nonlinear Problems . . . . .	13
<b>3</b>	<b>Near-field Imaging of the Surface Displacement on an Infinite Ground Plane . . . . .</b>	<b>15</b>
3.1	Forward and Inverse Scattering Problems . . . . .	15
3.2	Analysis of the Scattered Wave . . . . .	18
3.2.1	Layer Potential and Boundary Integral Equations . . . . .	18
3.2.2	Scattered Wave in Near-field Regime . . . . .	23
3.3	Near-field Imaging . . . . .	27
3.3.1	Inversion Method . . . . .	27
3.3.2	Fréchet Differentiability of the Nonlinear Operator . . . . .	32
3.4	Numerical Examples . . . . .	39
3.5	Discussions . . . . .	44
<b>4</b>	<b>Imaging with Multiple Frequency Data . . . . .</b>	<b>45</b>
4.1	Introduction . . . . .	45
4.1.1	Problem Formulations . . . . .	45
4.1.2	Why Multiple Frequency Data . . . . .	47
4.2	Analysis of the Forward Scattering Problem . . . . .	47
4.2.1	Notations . . . . .	47
4.2.2	Dirichlet-to-Neumann Map . . . . .	49
4.2.3	Well-posedness of the Forward Scattering Problem in Bounded Domain . . . . .	51
4.3	Domain Derivative of the Forward Scattering Map . . . . .	53
4.4	Imaging with Multiple Frequency Data . . . . .	59
4.4.1	Descent Direction for the Cost Functional . . . . .	59
4.4.2	Reconstruction Scheme . . . . .	61
4.5	Numerical Examples . . . . .	64

4.5.1	Numerical approximation of the forward scattering problem . . . . .	64
4.5.2	Imaging of the local surface displacement . . . . .	65
<b>5</b>	<b>Conclusion . . . . .</b>	<b>75</b>
	<b>Bibliography . . . . .</b>	<b>78</b>

## LIST OF FIGURES

Images in this dissertation are presented in color

1.1	Evanescent wave. For interpretation of the references to color in this and all other figures, the reader is referred to the electronic version of this thesis. . . . .	2
3.1	Setup of the problem. . . . .	15
3.2	$e^{ik_2(\kappa)d}$ for $d \in (0, 1.5\lambda)$ when the spatial frequency $\kappa = 1.2k$ and $1.5k$ respectively . . . . .	27
3.3	$k_C/k$ versus the distance varying from $\lambda/10$ to $\lambda$ . . . . .	29
3.4	Real part (left) and the imaginary part (right) of the scattered field. .	40
3.5	Near-field (top) and far-field (bottom) images. The solid line represents the real image, and the dotted line is the reconstruction. . . . .	41
3.6	Relative error with respect to Newton iterations. . . . .	41
3.7	Near-field (left) and far-field (right) images. The solid line represents the real image, and the dotted line is the reconstruction. . . . .	42
3.8	Real profile, the distance between neighboring bumps is $\lambda/10$ . . . . .	42
3.9	Comparison of the reconstruction (dotted line) with the real profile (solid line) for the near-field case. . . . .	43
4.1	Problem geometry. . . . .	46

4.2	Top: real profile. Bottom: reconstruction (dash line) at $k = 16$ compared with the real curve (solid line). . . . .	67
4.3	Relative error with respect to the wavenumber. . . . .	68
4.4	Evolution of the reconstruction at $k = 1, 5, 8, 10, 12, 16$ (dash line, left to right, top to bottom). . . . .	69
4.5	Top: relative residual with respect to the iteration number at $k = k_M$ when only single frequency data is used. Bottom: reconstruction (dash line) with single frequency only. . . . .	70
4.6	Reconstruction (dash line) at $k = 30$ compared with the real curve (solid line). . . . .	71
4.7	Relative error with respect to the wavenumber. . . . .	72
4.8	Reconstruction (dash line) at $k = 16$ compared with the real curve (solid line). . . . .	72
4.9	Reconstruction at $k = 10, 20, 33, 40$ (dash line, top to bottom) compared with the real curve (solid line). . . . .	73

# Chapter 1

## Introduction

### 1.1 Near-field Optics

Near-field optics is the study of the evanescent wave fields and their interactions with matter on a sub-wavelength scale. Usually the evanescent fields are localized to the optical source region or the surface of the scattering object, and the study of the near-field optics is mostly concerned with the localized region within one wavelength. The modern interests on the topic was mainly motivated by its applications in near-field imaging microscopies. We refer the reader to [51, 62] and the references therein for detailed discussions.

The study of the near-field optics has its origin in an effort to break the diffraction limit imposed by the far-field imaging. In far-field optics, the cut-off of the spatial spectrum is very strict: only the propagating wave components with spatial frequency below the wavenumber can be used. The loss of higher spatial frequencies leads to the diffraction limit, which is also known as the Rayleigh resolution limit. At the end of the nineteenth century, Abbe and Rayleigh [1, 53] derived a criterion for this limit. The minimum distance  $\Delta x$  between two point sources at which they can still

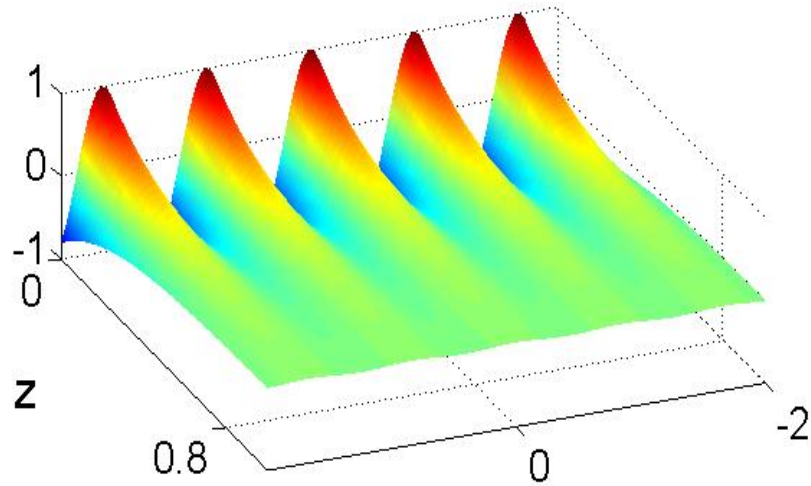


Figure 1.1: Evanescent wave. For interpretation of the references to color in this and all other figures, the reader is referred to the electronic version of this thesis.

be unambiguously distinguished as two separate sources reads as

$$\Delta x = 0.61\lambda/NA,$$

where  $NA$  is the numerical aperture, and the best possible  $NA$  for optical glasses is roughly 1.5. Therefore, the spatial resolution for a far-field optical microscopy is approximately  $\frac{\lambda}{2}$ . In near-field optics, however, the bandwidth of spatial frequency is expanded by taking account of the evanescent waves.

The evanescent waves can be described by plane waves of the form  $e^{i(\mathbf{k}\cdot\mathbf{x}-\omega t)}$ , where at least one component of the wave vector  $\mathbf{k}$  describing the direction of propagation is imaginary. They play a central role in near-field optics. In the spatial direction defined by the imaginary component of  $\mathbf{k}$ , the wave no longer propagates, but decays exponentially. Figure 1.1 is the plot of an evanescent wave that propagates in the  $xy$  plane, but decays exponentially in the  $z$  direction.

In fact, the total internal reflection at the surface of a dielectric medium generates

such an evanescent wave. Let us consider a plane wave impinging on a flat surface between two media characterized by the refraction index  $n_1$  and  $n_2$  respectively and  $n_1 > n_2$ . By the boundary conditions on the interface, the wave vectors  $\mathbf{k}_1$  and  $\mathbf{k}_2$  in the two media take the form of

$$\begin{aligned}\mathbf{k}_1 &= (k_x, k_y, k_{z1}), & |\mathbf{k}_1| &= \frac{n_1\omega}{c}, \\ \mathbf{k}_2 &= (k_x, k_y, k_{z2}), & |\mathbf{k}_2| &= \frac{n_2\omega}{c}.\end{aligned}$$

Here  $c$  is the speed the light in the vacuum. If the incident angle  $\theta_i$  is the larger than the critical angle  $\theta_c = \arcsin \frac{n_2}{n_1}$ , then  $k_{z2}$  becomes imaginary, and the exponential decay constant is  $|\mathbf{k}_2| \sqrt{(\frac{n_1}{n_2})^2 \sin^2 \theta_i - 1}$ .

The evanescent waves are always restricted to the surfaces of imaging objects, thus the study of the optical interactions on a subwavelength scale becomes very significant. This usually complicates the analysis as well as the computation — the price we have to pay for the inclusion of evanescent waves to obtain images with better spatial resolution.

## 1.2 Near-field Imaging Microscopy

The central idea of near-field microscopies is to retain the spatial frequencies associated with evanescent waves, thereby increasing the bandwidth of spatial frequencies. In principle, arbitrary resolution can be achieved provided the bandwidth is infinite. However, this is at the expense of strong coupling between the source and the imaging object. Here we briefly summarize several existing near-field imaging modalities, and refer to the monograph [51] and [30, 25, 26, 54] for references. The list is of course by no means to be complete.

Near-field scanning optical microscopy (NSOM) [51, 25, 30] applies the excitation

beam emanating from a tiny aperture (e.g., pointed optical fiber) or a tiny metal tip. The electric field distribution changes significantly as the aperture size becomes smaller. In particular, when the aperture size is below the wavelength, the  $z$  component of the wave vector becomes imaginary. The strong localization of such evanescent waves yields the subwavelength resolution that can be achieved in near-field scanning optical microscopy.

The scanning tunneling optical microscope (STOM) [26], also called the phonon scanning tunneling microscope (PSTM) [54] uses far-field illumination and near-field detection. To illuminate the sample, a laser beam undergoes total internal reflection at the surface of the sample support. A bare tapered glass fiber is dipped into this evanescent field to locally couple some of the light into the probe where it is converted into propagating modes that are guided towards a detector.

There are other imaging modalities such as the near-field illumination and near-field detection configuration which makes use of near-field interactions for both excitation and detection, and the energy-transfer microscopy where the near-field interaction between probe and sample is achieved through dipole-dipole coupling. There are new methods being developed continuously. Apparently large diversity of methods are usually categorized according to their specific illumination and detection conditions, and in practice, it is usually desirable to have different specialized modalities combined together to give more efficient imaging.

### **1.3 Near-field Imaging via Inverse Scattering**

In an optical microscopy, the object is usually visualized in an analogical way with little or no numerical treatment. Therefore, the images of the scattering object is usually problematic [18, 47]. There is an alternative type of near-field imaging technique which relies entirely on a numerical inversion procedure to reconstruct the sample

from the data of the scattered field, i.e., to solve the inverse scattering problem.

In [15], M. Bertero, P. Boccacci and M. Piana discussed the concept of resolution for the inverse diffraction problems that arise in the acoustic holography. They showed that the super-resolution is possible due to the information conveyed by evanescent waves in near-field.

P. Carney and J. Schotland also studied the inverse scattering problem for the near-field microscopy and three-dimensional total internal reflection microscopy (TIRM). They also showed subwavelength spatial resolution [19, 20]. Their framework on the near-field imaging is all based on the weak-scattering approximation (or Born approximation).

More recently, A. Sentenac *et al* carried out the whole nonlinear inversion process for the total internal reflection microscopy [5, 6]. Unfortunately, in optics the highest refractive index available for the prism function in TIRM is close to two, which limits the spatial frequency of illuminating field. In order to increase the spatial frequencies of the illuminating field beyond that reachable with a prism, they proposed to deposit the sample on an optimized grating [21]. This is the so called grating-assisted optical diffraction tomography.

The starting point of this thesis is also based on the idea of imaging by applying the inverse scattering theory. We study the inverse diffraction problem for an unbounded obstacle which is a ground plane with some local disturbance. New numerical schemes are developed to reconstruct the surface displacement from the boundary measurements.

In Chapter 2, we briefly summarize the mathematical theories of inverse problems, which serves as the building blocks for the study of the inverse scattering problem.

Chapter 3 is devoted to the analysis the scattered field in near-field regime, and the design a numerical method that makes use of the evanescent modes effectively to improve the resolution of the near-field image. Most of Chapter 3 comes from [10].

In Chapter 4, we use multiple frequency data to image the profile of the surface displacement. A stable and accurate reconstruction method is presented and investigated with numerical simulations. In particular, for a multiple scale profile, the proposed method resolves the fine scales with sufficiently high frequency information. Chapter 4 is mostly extracted from [11].

# Chapter 2

## Mathematical Theory of Inverse Problem

In this chapter, we briefly summarize the mathematical theories for the inverse problems, with focus on the linear compact operators in Hilbert spaces. It is intended as an introduction to the basic ideas on the ill-posed problems and regularization methods for their solutions. We refer to the monographs [31, 43, 24, 37] and references therein for detailed discussions.

### 2.1 Concepts of Ill-Posed Problem

In his lecture published in [38], Hadamard claims that a mathematical model for a physical problem has to be properly posed or well-posed in the sense that it has following properties:

- There exists a solution of the problem (existence).
- There exists at most one solution of the problem (uniqueness).
- The solution depends continuously on the data (stability).

If any of the above three criteria is violated, the problem is called ill-posed. In practice, the instability is one of the primary interest in the study of ill-posed problems. The violations of stability always creates serious numerical problems: an infinitesimal noise in the measurement will give rise to large errors in the solution. No mathematical trick can make an inherently unstable problem stable. A remedy is to use the regularization methods. But all that a regularization method can do is to recover partial information of the solution as stable as possible.

Consider the operator equation

$$Kx = y, \tag{2.1}$$

where  $K$  is an operator between Hilbert spaces  $X$  and  $Y$ . The typical example of an ill-posed problem is when  $K$  is a compact operator, since the inverse  $K^{-1}$  is unbounded. We will base our exposition on (2.1) in the following sections.

## 2.2 Singular Value Decomposition for Linear Compact Operators

A better way to understand the structure of linear compact operator  $K$  ( $X \rightarrow Y$ ) is from the spectral theory. For an self-adjoint operator  $K$ , all of its eigenvalues are real. Moreover,  $K$  has at least one but at most a countable number of eigenvalues with 0 as the only possible accumulation point.

Assume that the sequences  $\{\lambda_n\}_{n=1}^{\infty}$  of the nonzero eigenvalues is ordered such that

$$|\lambda_1| \geq |\lambda_2| \geq |\lambda_3| \geq \cdots$$

Let  $x_n$  be a sequence of corresponding orthonormal eigenvectors. Then for  $x \in X$ ,

$$Kx = \sum_{n=1}^{\infty} \lambda_n(x, x_n)x_n.$$

For a proof of this spectral decomposition for self adjoint operators, see for example [45].

The spectral theorem for compact self-adjoint operators has an extension to nonself-adjoint operators. If  $K : X \rightarrow Y$  is a linear compact operator, then its adjoint operator  $K^* : Y \rightarrow X$  is also compact. We call the nonnegative square roots of the eigenvalues for the self-adjoint compact operator  $K^*K$  the singular values.

**Theorem 2.2.1.** (*Singular Value Decomposition*) *Let  $K : X \rightarrow Y$  be a linear compact operator,  $K^* : Y \rightarrow X$  be its adjoint operator, and  $\mu_1 \geq \mu_2 \geq \mu_3 \cdots > 0$  be ordered sequences of the positive singular values of  $K$ . Then there exist orthonormal systems  $\{x_n\}_{n=1}^{\infty} \subset X$  and  $\{y_n\}_{n=1}^{\infty} \subset Y$  with the following properties:*

$$Kx_n = \mu_n y_n \quad \text{and} \quad K^*y_n = \mu_n x_n \quad \text{for all } n \in \mathbb{N}.$$

*The system  $(\mu_n, x_n, y_n)$  is called a singular system for  $K$ . For each  $x \in X$ , there exists a singular value decomposition*

$$x = x_0 + \sum_{n=1}^{\infty} (x, x_n)x_n$$

*for some  $x_0 \in \text{Ker}(K)$  and*

$$Kx = \sum_{n=1}^{\infty} \mu_n (x, x_n)y_n.$$

The following theorem expresses the solution to the equation  $Kx = y$  in terms of the singular system.

**Theorem 2.2.2.** (*Picard*) Let  $K : X \rightarrow Y$  be a linear compact operator with the singular system  $(\mu_n, x_n, y_n)$ . The solution to

$$Kx = y$$

is solvable if and only if  $f \in (\text{Ker}(K^*))^\perp$  and

$$\sum_{n=1}^{\infty} \frac{1}{\mu_n^2} |(y, y_n)|^2 < \infty.$$

In this case

$$x = \sum_{n=1}^{\infty} \frac{1}{\mu_n} (y, y_n) x_n.$$

Picard's theorem demonstrate the ill-posed nature of the equation  $Kx = y$ . If we perturb the right hand side by  $\delta y$ , the perturbation of the solution  $x$  can be made arbitrarily large due to the fact that the singular values tend to zero.

## 2.3 Regularization Methods for Linear Problems

Since the inverse of the operator  $K$  is not bounded, one remedy is to use the regularization methods. A regularization strategy is a family of linear and bounded operators

$$R_\alpha : Y \rightarrow X, \quad \alpha > 0$$

such that

$$\lim_{\alpha \rightarrow 0} R_\alpha Kx = x \quad \text{for all } x \in X.$$

Let  $y^\delta$  be the measured data (with error) with  $\|y - y^\delta\| \leq \delta$ , then

$$x^{\alpha, \delta} := R_\alpha y^\delta$$

is an approximation of the solution of (2.1). The error  $\|x - x^\delta\|$  can be split into two parts:

$$\delta \|R_\alpha\| \quad \text{and} \quad \|R_\alpha Kx - x\|,$$

where the first term describes the error in the data multiplied by  $\|R_\alpha\|$  and the second term denotes the approximation error  $\|(R_\alpha - K^{-1})y\|$ . The art of choosing the regularization parameter  $\alpha$  will always be to find the right compromise between accuracy and stability.

A convenient way to construct admissible regularization strategies is given by filtering singular value systems. The idea of using filters has a long history and is very convenient for theoretical purposes [36, 58]. Let  $(\mu_n, x_n, y_n)$  be a singular system for  $K$ . The regularization strategy is constructed by damping the factors  $1/\mu_n$ .

**Theorem 2.3.1.** *(Regularization by damping [43]) Let  $K : X \rightarrow Y$  be a linear compact operator with singular system  $(\mu_n, x_n, y_n)$ .*

$$q : (0, \infty) \times (0, \|K\|) \rightarrow \mathbb{R}$$

is a function with the following properties:

- $|q(\alpha, \mu)| \leq 1$  for all  $\alpha > 0$  and  $0 < \mu < \|K\|$ .
- For each  $\alpha > 0$  there exists  $c(\alpha)$  such that

$$|q(\alpha, \mu)| \leq c(\alpha)\mu \quad \text{and} \quad 0 < \mu \leq \|K\|.$$

- $\lim_{\alpha \rightarrow 0} q(\alpha, \mu) = 1$  for each  $0 < \mu < \|K\|$ .

Then the operator  $R_\alpha : Y \rightarrow X$ , defined by

$$x = R_\alpha y = \sum_{n=1}^{\infty} \frac{q(\alpha, \mu_n)}{\mu_n} (y, y_n) x_n$$

is a regularization strategy with  $\|R_\alpha\| \leq c(\alpha)$ . The function  $q$  is called a regularizing filter for  $K$ .

There are various choices of the function  $q$  that satisfies the above properties. Typically, we list three filter functions as follows:

(1)  $q$  is defined by

$$q(\alpha, \mu) = \begin{cases} 1, & \mu^2 \geq \alpha, \\ 0, & \mu^2 < \alpha. \end{cases}$$

This choice of  $q$  is also known as the spectral cutoff.

(2)  $q(\alpha, \mu) = \mu^2/(\alpha + \mu^2)$ . This choice of the filter function  $q$  is equivalent to the Tikhonov regularization strategy [59, 60]. The Tikhonov regularization tries to minimize the functional

$$J_\alpha(x) := \|Kx - y\| + \alpha \|x\|,$$

and the minimum  $x^\alpha$  of the Tikhonov functional is the unique solution of the normal equation

$$\alpha x^\alpha + K^* K x^\alpha = K^* y.$$

It is clear that the solution  $x^\alpha$  can be written in the form  $x^\alpha = R_\alpha y$  with

$$R_\alpha := (\alpha I + K^* K)^{-1} K^* = \sum_{n=1}^{\infty} \frac{\mu_n}{\alpha + \mu_n^2} (\cdot, y_n) x_n.$$

(3)  $q(\alpha, \mu) = 1 - (1 - \alpha\mu^2)^{1/\alpha}$ . This choice of the filter function  $q$  leads to the so-called Landweber iteration method [16, 35, 48]. The iteration scheme is the steepest descent algorithm for the quadratic functional  $x \rightarrow \|Kx - y\|^2$ , where

$x^m$  is computed recursively by

$$x^m = x^{m-1} - aK^*(Kx^{m-1} - y), \quad m = 1, 2, \dots$$

The resulting regularized operator has the form

$$R_m := a \sum_{j=0}^{m-1} (I - aK^*K)^j K^* = \sum_{n=1}^{\infty} \frac{1 - (1 - a\mu_n^2)^m}{\mu_n} (\cdot, y_n) x_n.$$

There are many other regularization strategies for the solution of the linear ill-posed problems, for example, the conjugate gradient method [27], the regularization by discretization [14, 45], etc.

One important issue for the regularization strategy is the choice of the regularization parameter  $\alpha$  such that the accuracy and stability are balanced. In practice, usually the posteriori parameter choice rules are applied. One of the most widely used strategies is the so-called discrepancy principle due to Morozov [49]. We also refer to [31, 43] for the discussions of other posteriori rules to choose the regularization parameter.

## 2.4 Regularization Methods for Nonlinear Problems

Let  $F$  be a nonlinear operator between Hilbert spaces  $X$  and  $Y$ , and we want to solve

$$F(x) = y. \tag{2.2}$$

The regularization theory for the nonlinear ill-posed problem (2.2) is by far not so well developed as in the linear case.

As in the linear case, the Tikhonov regularization minimizes the functional

$$\|F(x) - y\| + \alpha \|x\|. \quad (2.3)$$

The minimization problem (2.3) admits a solution, though the solution may not be unique in general. Moreover, the Tikhonov regularization strategy is stable in the sense of continuous dependence of the solution on the data  $y$  [31, 55]. If  $y$  in (2.3) is replaced by the perturbed data  $y^\delta$ , then the corresponding solution  $x^{\alpha, \delta}$  of (2.3) converges to the minimum norm solution of (2.2) for general nonlinear problems when  $\delta \rightarrow 0$  [55]. The rates of convergence are presented in [32, 50].

The nonlinear Landweber iteration to the nonlinear ill-posed problem updates the solution along the steepest descent direction of the functional  $\|F(x) - y\|$ :

$$x^m = x^{m-1} - \alpha F'(x^{m-1})^*(F(x^{m-1}) - y), \quad m = 1, 2, \dots$$

For nonlinear problems, the iteration will not have a global convergence property. However, under suitable condition on the nonlinear operator  $F$  with an appropriate stopping rule, the convergence is obtained in [39].

There are also Newton's type methods for solving (2.2). The main idea is to repeatedly linearize the nonlinear operator equation by solving

$$F'(x^{m-1})(x - x^{m-1}) = y - F(x^{m-1}).$$

Usually  $F'(x^{m-1})$  is compact, and regularization strategy is applied when solving the linearized problem. We refer to [31] for detailed discussions.

# Chapter 3

## Near-field Imaging of the Surface Displacement on an Infinite Ground Plane

### 3.1 Forward and Inverse Scattering Problems

Consider the scattering of the time harmonic electromagnetic wave that impinges on an unbounded obstacle. The boundary of the obstacle is assumed to be a perturbation

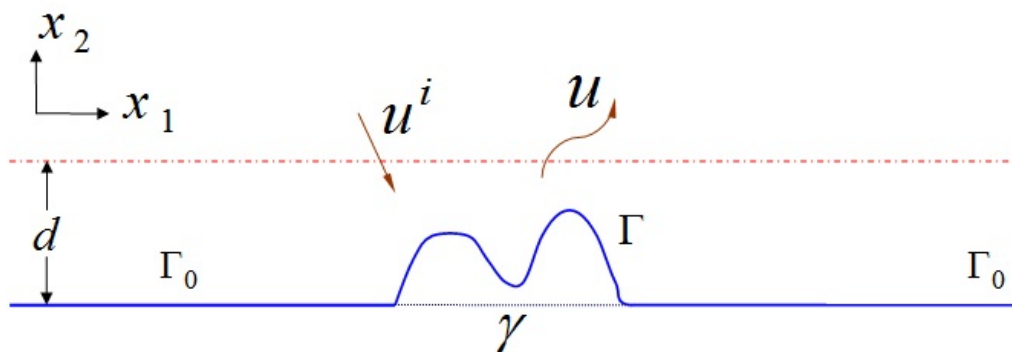


Figure 3.1: Setup of the problem.

of the  $x_1x_3$  plane. It is also assumed that the surface displacement is invariant along the  $x_3$  direction, and is local with respect to  $x_1$ . We further restrict the study to the TM polarization or E-parallel case, i.e., the electric field  $E = (0, 0, u(x_1, x_2))$ . Consequently, the Maxwell equations are reduced to the two dimensional Helmholtz equation.

Before introducing the forward scattering model, we describe the geometry of the obstacle shown in Figure 3.1. Let  $\gamma \subset \mathbb{R}$  be bounded, open, and  $\partial\gamma$  be the boundary of  $\gamma$ . Denote the closure of  $\gamma$  as  $\bar{\gamma}$ . The ground plane  $\Gamma_0 := \mathbb{R} \setminus \gamma$ , and the local surface displacement is represented by  $\Gamma := \{x = (x_1, x_2) \mid x_1 \in \gamma, x_2 = f(x_1)\}$ , where the function  $f$  is defined on  $\bar{\gamma}$ :

$$f(x_1) > 0 \text{ for } x_1 \in \gamma, \quad f(x_1) = 0 \text{ for } x_1 \in \partial\gamma.$$

By requiring  $f > 0$  on  $\gamma$ , the surface displacement is directed upward. Clearly,  $\partial D := \Gamma \cup \Gamma_0$  is the boundary of the whole unbounded obstacle on which the electromagnetic wave impinges. The domain above  $\partial D$  is denoted as  $D \subset \mathbb{R}^2$ .

The incident wave field  $u^i = e^{ikq \cdot x}$  is a plane wave that propagates along the direction  $q = (\sin \theta, -\cos \theta)^T$ , where  $\theta$  is the incident angle and  $k = \frac{\omega}{c}$  is the wavenumber. Here  $\omega$  is the angular frequency, and  $c$  is the speed of the wave propagating in the vacuum. Let  $\lambda = \frac{2\pi}{k}$  denote the wavelength. If the obstacle is a flat perfect conductor, then the reflected field  $u^r = -e^{ikq' \cdot x}$  produced by the flat surface is a plane wave propagating along the direction  $q' = (\sin \theta, \cos \theta)^T$ . In general, the total field  $u^t$  from the scattering by  $\Gamma \cup \Gamma_0$  consists of three parts: the incident wave  $u^i$ , the reflected wave  $u^r$ , and the scattered field. The scattered field  $u$  satisfies the Helmholtz equation

$$\Delta u + k^2 u = 0 \quad \text{in } D. \tag{3.1}$$

Assuming that the obstacle is a perfect conductor, the total field vanishes on the

boundary. Hence

$$u = -(u^i + u^r) \quad \text{on } \partial D. \quad (3.2)$$

It is easily seen that  $u = 0$  on  $\Gamma_0$ . Moreover, the scattered field satisfies the Sommerfeld radiation condition:

$$\lim_{r \rightarrow \infty} \sqrt{r} \left( \frac{\partial u}{\partial r} - iku \right) = 0, \quad r = |x|. \quad (3.3)$$

The forward scattering problem (4.1)-(4.3) admits a unique solution  $u \in C^2(D) \cap C(\bar{D})$  if  $\partial D$  is  $C^2$  and boundary data  $u|_{\partial D}$  is continuous [61]. Clearly here the plane wave  $u^i, u^r \in C^\infty(\mathbb{R}^2)$ . It is worth mentioning that there are many results on related scattering problems in the literature. The well-posedness of the scattering problem for an obstacle with locally downward surface displacement ( $f(x_1) < 0$  for  $x_1 \in \gamma$ ) was studied in [3, 4]. There are also general studies on the scattering by a non-local perturbed half plane. See for example [64] and the references therein.

In our framework for the inverse scattering problem, data is collected on the line  $x_2 = d$  above the surface displacement with a distance that is smaller than the wavelength  $\lambda$  (near-field regime). To be more precise, it is required that  $0 < d - \max_{x_1 \in \bar{\gamma}} f(x_1) < \lambda$ . The inverse problem is to reconstruct  $f$  from the scattered field  $u(\cdot, d)$  collected on the line  $x_2 = d$ . Our work is originally motivated by the recent paper [29], in which a linearized model has been introduced for the nonlinear inverse scattering problem by the single scattering assumption. The authors also proposed a broadband imaging strategy for denoising and improving the resolution of the image. However, this linearized model is valid only if  $\frac{f}{\lambda} \ll 1$  and the modulus of its derivative  $|f'| \ll 1$  simultaneously. Here we investigate the more general case by considering the full scattering model, for which the linearized model in [29] is no longer valid. For the reconstruction of the star-like local disturbance from the far field pattern of the scattered field, we refer to [46].

This imaging problem shares many of the well-known difficulties with other inverse boundary value problems, particularly nonlinearity and ill-posedness. However, by collecting data in the near-field regime, the evanescent wave modes which are not accessible in the far-field regime ( $d - \max f \gg \lambda$ ) become significant. This crucial fact may be confirmed by the analysis of the scattered field in Section 3.2. Evanescent wave modes make it possible to break the diffraction limit. It is shown that such exponentially decayed modes of the scattered wave contain exactly the high spatial frequency information (fine features) of the profile  $f$ . Our study is to analyze the scattered field carefully, and design a numerical method that makes use of the evanescent modes effectively, thus to improve the resolution of the image. Numerical examples confirm that a resolution of  $\lambda/10$  is obtained in the near field.

## 3.2 Analysis of the Scattered Wave

### 3.2.1 Layer Potential and Boundary Integral Equations

Introduce Green's function

$$G(x, y) := \Phi(x, y) - \Phi(x_r, y),$$

where  $\Phi(x, y) = \frac{i}{4}H_0^{(1)}(k|x - y|)$  is the fundamental solution for the Helmholtz equation in  $\mathbb{R}^2$  and  $x_r$  is the reflection of  $x$  by the  $x_1$  axis, i.e.,  $x_r = (x_1, -x_2)$ .

Denote  $\bar{\Gamma} = \Gamma \cup \partial\gamma$ ,  $\Gamma_r := \{ (x_1, -x_2) \mid x \in \Gamma \}$ ,  $\overline{\Gamma \cup \Gamma_r} = \Gamma \cup \Gamma_r \cup \partial\gamma$ , and  $D_r := \{ (x_1, -x_2) \mid x \in D \}$ . For a function  $\psi \in C(\bar{\Gamma})$ , we define the single layer potential:

$$u(x) = \int_{\bar{\Gamma}} G(x, y)\psi(y)dsy, \quad x \in \mathbb{R}^2 \setminus \overline{\Gamma \cup \Gamma_r}.$$

The following lemma is concerned with the limit of the normal derivative of the single

layer potential, when it is extended from above and below the boundary  $\Gamma$ . The limit for the case when  $\Gamma$  is the smooth boundary of a bounded obstacle is well known [23, 24]. Here  $\Gamma$  is not a closed curve. For completeness, the proof of the lemma is provided.

**Lemma 3.2.1.** *Assume that  $\Gamma$  is  $C^2$ . For the single layer potential with continuous density  $\psi$ , the following holds:*

$$\left(\frac{\partial u}{\partial \nu}\right)_{\pm}(x) = \int_{\Gamma} \frac{\partial G(x, y)}{\partial \nu_x} \psi(y) ds_y \mp \frac{1}{2} \psi(x), \quad x \in \Gamma,$$

where  $\nu$  is the unit normal directed into  $D$ ,  $\left(\frac{\partial u}{\partial \nu}\right)_{\pm}(x) := \lim_{h \rightarrow 0^+} \nu(x) \cdot \nabla u(x \pm h\nu(x))$ .

**Proof.** For  $x \in \Gamma$ ,  $\epsilon > 0$ , denote  $\Gamma_{x, \epsilon} := \{y \in \Gamma, |y - x| < \epsilon\}$ . We first show that

$$\lim_{\epsilon \rightarrow 0} \lim_{h \rightarrow 0^+} \int_{\Gamma_{x, \epsilon}} \frac{\partial \Phi(x + h\nu_x, y)}{\partial \nu_x} ds_y = -\frac{1}{2}.$$

Let  $\partial\Omega$  (the boundary of some bounded connected domain  $\Omega$ ) be a  $C^2$  closed curve such that  $\Gamma \subset \partial\Omega$ . Moreover, for  $x \in \Gamma$ , the unit outward normal of  $x$  on  $\partial\Omega$  coincides with  $\nu_x$ . Let  $\psi \equiv 1$  on  $\partial\Omega$ , from the classical results in [23, 24],

$$\left(\frac{\partial u}{\partial \nu}\right)_{+}(x) = \int_{\partial\Omega} \frac{\partial \Phi(x, y)}{\partial \nu_x} ds_y - \frac{1}{2}, \quad x \in \Gamma. \quad (3.4)$$

On the other hand, for any small fixed number  $\epsilon > 0$ ,

$$\begin{aligned} \lim_{h \rightarrow 0^+} \int_{\partial\Omega} \frac{\partial \Phi(x + h\nu_x, y)}{\partial \nu_x} ds_y &= \lim_{h \rightarrow 0^+} \left[ \int_{\partial\Omega \setminus \Gamma_{x, \epsilon}} \frac{\partial \Phi(x + h\nu_x, y)}{\partial \nu_x} ds_y + \int_{\Gamma_{x, \epsilon}} \frac{\partial \Phi(x + h\nu_x, y)}{\partial \nu_x} ds_y \right] \\ &= \int_{\partial\Omega \setminus \Gamma_{x, \epsilon}} \frac{\partial \Phi(x, y)}{\partial \nu_x} ds_y + \lim_{h \rightarrow 0^+} \int_{\Gamma_{x, \epsilon}} \frac{\partial \Phi(x, y)}{\partial \nu_x} ds_y. \end{aligned}$$

Now letting  $\epsilon \rightarrow 0$ , we get

$$\lim_{h \rightarrow 0^+} \int_{\partial\Omega} \frac{\partial\Phi(x + h\nu_x, y)}{\partial\nu_x} ds_y = \int_{\partial\Omega} \frac{\partial\Phi(x, y)}{\partial\nu_x} ds_y + \lim_{\epsilon \rightarrow 0} \lim_{h \rightarrow 0^+} \int_{\Gamma_{x, \epsilon}} \frac{\partial\Phi(x, y)}{\partial\nu_x} ds_y. \quad (3.5)$$

From (3.4), (3.5), we have

$$\lim_{\epsilon \rightarrow 0} \lim_{h \rightarrow 0^+} \int_{\Gamma_{x, \epsilon}} \frac{\partial\Phi(x + h\nu_x, y)}{\partial\nu_x} ds_y = -\frac{1}{2}. \quad (3.6)$$

. For the integral on  $\Gamma$ , for any fixed small number  $\epsilon > 0$ ,

$$\begin{aligned} & \lim_{h \rightarrow 0^+} \int_{\bar{\Gamma}} \frac{\partial\Phi(x + h\nu_x, y)}{\partial\nu_x} \psi(y) ds_y \\ = & \lim_{h \rightarrow 0^+} \int_{\bar{\Gamma} \setminus \Gamma_{x, \epsilon}} \frac{\partial\Phi(x + h\nu_x, y)}{\partial\nu_x} \psi(y) ds_y + \lim_{h \rightarrow 0^+} \int_{\Gamma_{x, \epsilon}} \frac{\partial\Phi(x + h\nu_x, y)}{\partial\nu_x} ds_y \psi(x) \\ & + \lim_{h \rightarrow 0^+} \int_{\Gamma_{x, \epsilon}} \frac{\partial\Phi(x + h\nu_x, y)}{\partial\nu_x} (\psi(y) - \psi(x)) ds_y \\ = & \int_{\bar{\Gamma} \setminus \Gamma_{x, \epsilon}} \frac{\partial\Phi(x, y)}{\partial\nu_x} \psi(y) ds_y + \lim_{h \rightarrow 0^+} \int_{\Gamma_{x, \epsilon}} \frac{\partial\Phi(x + h\nu_x, y)}{\partial\nu_x} ds_y \psi(x) \\ & + \lim_{h \rightarrow 0^+} \int_{\Gamma_{x, \epsilon}} \frac{\partial\Phi(x + h\nu_x, y)}{\partial\nu_x} (\psi(y) - \psi(x)) ds_y. \end{aligned}$$

On the other hand, there exists some constant  $M$  that

$$\left| \int_{\Gamma_{x, \epsilon}} \frac{\partial\Phi(x + h\nu_x, y)}{\partial\nu_x} ds_y \right| \leq M$$

and

$$|\psi(y) - \psi(x)| \rightarrow 0, \quad \text{as } \epsilon \rightarrow 0 \quad \text{for } y \in \Gamma_{x, \epsilon}.$$

Therefore, by letting  $\epsilon \rightarrow 0$  and noting (3.6), we obtain

$$\lim_{h \rightarrow 0^+} \int_{\bar{\Gamma}} \frac{\partial\Phi(x + h\nu_x, y)}{\partial\nu_x} \psi(y) ds_y = \int_{\bar{\Gamma}} \frac{\partial\Phi(x, y)}{\partial\nu_x} \psi(y) - \frac{1}{2} \psi(x).$$

For  $x \in \Gamma$ ,

$$\lim_{h \rightarrow 0^+} \int_{\bar{\Gamma}} \frac{\partial \Phi(xr + h\nu x, y)}{\partial \nu x} \psi(y) ds_y = \int_{\bar{\Gamma}} \frac{\partial \Phi(xr, y)}{\partial \nu x} \psi(y).$$

By combining the above, we have

$$\left( \frac{\partial u}{\partial \nu} \right)_+ (x) = \int_{\bar{\Gamma}} \frac{\partial G(x, y)}{\partial \nu x} \psi(y) ds_y - \frac{1}{2} \psi(x), \quad x \in \Gamma.$$

The proof for  $\left( \frac{\partial u}{\partial \nu} \right)_-$  can be carried out in the same fashion.  $\square$

The following representation result may serve as a starting point for the analysis of the scattered field.

**Lemma 3.2.2.** *If  $\partial D$  is  $C^3$ , then there exists  $\psi \in C(\bar{\Gamma})$  such that the solution to (4.1)-(4.3) can be expressed as the single layer potential*

$$u(x) = \int_{\bar{\Gamma}} G(x, y) \psi(y) ds_y \quad x \in D. \quad (3.7)$$

**Proof.** Let  $u$  be the solution of (4.1)-(4.3). Note  $u = 0$  on  $\Gamma_0$ , by Green's theorem and the radiation condition, the scattered field takes the following form

$$u(x) = \int_{\bar{\Gamma}} \frac{\partial G(x, y)}{\partial \nu y} u(y) - G(x, y) \frac{\partial u(y)}{\partial \nu y} ds_y, \quad x \in D. \quad (3.8)$$

Denote the domain bounded by  $\bar{\Gamma} \cup \bar{\Gamma}_r$  as  $\tilde{D}$ . Let  $u_0 := u^i + u^r$ . Then  $u_0 \in C^\infty(\mathbb{R}^2)$  satisfies the Helmholtz equation in  $\tilde{D}$ . By Green's theorem, we have

$$\left( \int_{\bar{\Gamma}} + \int_{\bar{\Gamma}_r} \right) \left( \frac{\partial \Phi(x, y)}{\partial \nu y} u_0(y) - \Phi(x, y) \frac{\partial u_0(y)}{\partial \nu y} \right) ds_y = 0, \quad x \in D, \quad (3.9)$$

where  $\nu_y$  is the unit normal directed to  $D$  for  $y \in \bar{\Gamma}$ ,  $\nu_y$  is the unit normal directed to  $D_r$  for  $y \in \bar{\Gamma}_r$ .

By noting that  $u_0(y) = -u_0(y_r)$ , and  $\frac{\partial u_0(y)}{\partial \nu_y} = -\frac{\partial u_0(y_r)}{\partial \nu_{y_r}}$  for  $y \in \bar{\Gamma}$ , we get

$$\begin{aligned} \int_{\bar{\Gamma}_r} \frac{\partial \Phi(x, y)}{\partial \nu_y} u_0(y) ds_y &= \int_{\bar{\Gamma}} \frac{\partial \Phi(x_r, y)}{\partial \nu_y} (-u_0(y)) ds_y, \\ \int_{\bar{\Gamma}_r} \Phi(x, y) \frac{\partial u_0(y)}{\partial \nu_y} ds_y &= \int_{\bar{\Gamma}} \Phi(x_r, y) \left(-\frac{\partial u_0(y)}{\partial \nu_y}\right) ds_y. \end{aligned} \quad (3.10)$$

Substituting (3.10) into (3.9) yields

$$\int_{\bar{\Gamma}} \frac{\partial G(x, y)}{\partial \nu_y} u_0(y) - G(x, y) \frac{\partial u_0(y)}{\partial \nu_y} ds_y = 0, \quad x \in D. \quad (3.11)$$

A combination of (3.8) and (3.11) leads to

$$\begin{aligned} u(x) &= \int_{\bar{\Gamma}} \frac{\partial G(x, y)}{\partial \nu_y} (u + u_0)(y) - G(x, y) \left( \frac{\partial u}{\partial \nu_y} + \frac{\partial u_0}{\partial \nu_y} \right) (y) ds_y, \\ &= - \int_{\bar{\Gamma}} G(x, y) \left( \frac{\partial u}{\partial \nu_y} + \frac{\partial u_0}{\partial \nu_y} \right) (y) ds_y. \quad x \in D. \end{aligned}$$

Let  $\psi = -\left(\frac{\partial u}{\partial \nu_y} + \frac{\partial u_0}{\partial \nu_y}\right)$ .  $\psi \in C(\bar{\Gamma})$  follows by the standard regularization theory for second-order elliptic equations and the Sobolev imbedding theorems [34]. The proof is now complete.  $\square$

Introduce the integral operator  $K : C(\bar{\Gamma}) \rightarrow C(\bar{\Gamma})$ ,

$$(K\psi)(x) := \int_{\bar{\Gamma}} G(x, y) \psi(y) ds_y, \quad x \in \bar{\Gamma}. \quad (3.12)$$

Denote  $g = -(u^i + u^r)|_{\bar{\Gamma}}$ . Then the existence of the solution to the integral equation  $K\psi = g$  follows from Lemma 3.2.2. Note that since the single layer potential can be continuously extended to  $\bar{\Gamma}$ , the density function  $\psi$  defined in Lemma 3.2.2 is a

solution of the integral equation  $K\psi = g$ . Regarding the uniqueness, we have the following result.

**Proposition 3.2.3.** *If  $\partial D$  is  $C^3$ , then  $K\psi = g$  is uniquely solvable if  $k^2$  is not the eigenvalue of  $-\Delta$  in  $\tilde{D}$  for the Dirichlet problem. Here  $\tilde{D}$  is the domain bounded by  $\overline{\Gamma \cup \Gamma_r}$ .*

**Proof.** If  $K\psi = 0$  for some  $\psi \in C(\overline{\Gamma})$ , then the single layer potential

$$u(x) = \int_{\overline{\Gamma}} G(x, y)\psi(y)ds_y$$

solves the exterior problem

$$\begin{cases} \Delta u_1 + k^2 u_1 = 0 & \text{in } D, \\ u_1 = 0 & \text{on } \partial D, \\ \lim_{r \rightarrow \infty} \sqrt{r} \left( \frac{\partial u_1}{\partial r} - iku_1 \right) = 0 \end{cases} \quad (3.13)$$

and the interior problem

$$\begin{cases} \Delta u_2 + k^2 u_2 = 0 & \text{in } \tilde{D}, \\ u_2 = 0 & \text{on } \overline{\Gamma \cup \Gamma_r}. \end{cases} \quad (3.14)$$

If  $k^2$  is not the eigenvalue of  $-\Delta$  in  $\tilde{D}$  for the Dirichlet problem, then (3.13) and (3.14) attains a unique solution respectively. Hence  $\frac{\partial u_1}{\partial v} - \frac{\partial u_2}{\partial v} = 0$ . By the jump condition in Lemma 3.2.1 we have  $-\psi = \frac{\partial u_1}{\partial v} - \frac{\partial u_2}{\partial v} = 0$  on  $\Gamma$ . Note that  $\psi \in C(\overline{\Gamma})$ , thus  $\psi \equiv 0$  on  $\overline{\Gamma}$ .  $\square$

### 3.2.2 Scattered Wave in Near-field Regime

Now we are ready to examine the scattered field in the near-field regime. We point out that the exponentially decayed (evanescent) wave modes which are localized to

the surface the local disturbance are significant in the near field, and formulate explicitly the connection between the evanescent wave modes and the high frequency components for the profile of the local disturbance.

For convenience, the Green's function  $G(x, y)$  and the fundamental solution  $\Phi(x, y)$  are written with an explicit dependence on the first variable:

$$G(x, y) = \tilde{G}(x_1 - y_1; x_2, y_2) := \tilde{\Phi}(x_1 - y_1, x_2 - y_2) - \tilde{\Phi}(x_1 - y_1, x_2 + y_2),$$

where  $\tilde{\Phi}(x_1, x_2) = \frac{i}{4} H_0^{(1)}(k\sqrt{x_1^2 + x_2^2})$ .

For the free space fundamental solution  $\tilde{\Phi}(x_1 - y_1, x_2 - y_2)$ , we have the following plane wave decomposition:

$$\tilde{\Phi}(x_1 - y_1, x_2 - y_2) = \frac{i}{4\pi} \int_{\mathbb{R}} \frac{1}{k_2(\kappa)} e^{i(x_1 - y_1) \cdot \kappa} e^{ik_2(\kappa)|x_2 - y_2|} d\kappa, \quad (3.15)$$

where

$$k_2(\kappa) = \begin{cases} \sqrt{k^2 - |\kappa|^2} & |\kappa| < k \quad (\text{propagating modes}), \\ i\sqrt{|\kappa|^2 - k^2} & |\kappa| > k \quad (\text{evanescent modes}). \end{cases} \quad (3.16)$$

The decomposition may be viewed as the sum of the plane waves that consist of propagating and evanescent modes. It is clear that all the wave modes propagate along the  $x_1$  direction. Along the  $x_2$  direction, when the magnitude of the spatial frequency  $|\kappa|$  is below  $k$ , the wave mode also propagates; otherwise, it decays exponentially along the  $x_2$  direction and is denoted as the evanescent mode.

A similar plane wave decomposition holds for  $\tilde{G}(x_1 - y_1; x_2, y_2)$  evaluated at  $x_2 = d$ :

$$\tilde{G}(x_1 - y_1; d, y_2) = \frac{i}{4\pi} \int_{\mathbb{R}} \frac{1}{k_2(\kappa)} e^{i(x_1 - y_1) \cdot \kappa} \left( e^{ik_2(\kappa)|d - y_2|} - e^{ik_2(\kappa)|d + y_2|} \right) d\kappa. \quad (3.17)$$

Thus for the scattered field at  $x = (x_1, d)$ , by noting the single layer potential (3.7),

some simple calculations yield

$$u(x_1, d) = \frac{i}{4\pi} \int_{\mathbb{R}} \int_{\bar{\gamma}} \frac{1}{k_2(\kappa)} e^{i(x_1 - y_1) \cdot \kappa} \left( e^{ik_2(\kappa)|d - f(y_1)|} - e^{ik_2(\kappa)|d + f(y_1)|} \right) \psi(y_1, f(y_1)) J dy_1 d\kappa,$$

where  $J = \sqrt{1 + |f'|^2}$ . This implies that the measured scattered field  $u$  on the line  $x_2 = d$  can also be viewed as the superposition of the propagating and evanescent wave modes. It is important to note that the evanescent modes with spatial frequency beyond the wavenumber  $k$  decay exponentially along the  $x_2$  direction, and are localized to the surface of the obstacle within one wavelength. Therefore, in the far-field regime, such evanescent modes carried by the scattered field are lost. However, in the near-field regime, the evanescent modes are significant, and the measured scattered field carries more information for the profile of the local disturbance to be reconstructed.

On the other hand, following from the Taylor expansion of  $\tilde{G}(x_1 - y_1; d, y_2)$  at  $y_2 = 0$ , the scattered field can also be expanded as

$$u(x_1, d) = \int_{\bar{\gamma}} [\tilde{G}(x_1 - y_1; d, 0) + \frac{\partial \tilde{G}(x_1 - y_1; d, 0)}{\partial y_2} f(y_1) + \frac{\partial^2 \tilde{G}(x_1 - y_1; d, 0)}{\partial y_2^2} (f(y_1))^2 + O(f^3)] \psi(y_1, f(y_1)) J dy_1.$$

where

$$(a) \quad \tilde{G}(x_1 - y_1; d, 0) = \frac{\partial^2 \tilde{G}(x_1 - y_1; d, 0)}{\partial y_2^2} = 0 \text{ by the symmetry property of } \tilde{G};$$

(b) for the high order term, by a direct calculation, asymptotically

$$O(f^3) = O\left(\left(\frac{f}{\lambda}\right)^2\right) \frac{\partial G(x_1 - y_1; d, 0)}{\partial y_2} f.$$

We assume that  $\left(\frac{f}{\lambda}\right)^2 \ll 1$ , and denote  $\varphi = \psi \sqrt{1 + |f'|^2}$ . Then the scattered

field is simplified as

$$\begin{aligned} u(x_1, d) &\approx \int_{\bar{\gamma}} \frac{\partial \tilde{G}(x_1 - y_1; d, 0)}{\partial y_2} f(y_1) \varphi(y_1) dy_1 \\ &= \int_{\mathbb{R}} \frac{\partial \tilde{G}(x_1 - y_1; d, 0)}{\partial y_2} f(y_1) \varphi(y_1) dy_1. \end{aligned} \quad (3.18)$$

The equality holds since the surface displacement is supported on  $\gamma$ . Here we implicitly extend the definition of  $f$  and  $\varphi$  to  $\mathbb{R}$  by setting  $f$  as 0 for  $x_1 \in \mathbb{R} \setminus \bar{\gamma}$ . On the other hand, from (3.17) a simple calculation yields

$$\frac{\partial \tilde{G}(x_1 - y_1; d, 0)}{\partial y_2} = \frac{1}{2\pi} \int_{\mathbb{R}} e^{i(x_1 - y_1) \cdot \kappa} e^{ik_2(\kappa)d} d\kappa.$$

Therefore, by taking the Fourier transform of (3.18), we arrive at

$$\hat{u}(\kappa, d) \approx e^{ik_2(\kappa)d} \widehat{(f\varphi)}(\kappa), \quad \kappa \in \mathbb{R}, \quad (3.19)$$

where  $\hat{\cdot}$  denotes the Fourier transform.

**Remark 2.1.** *The expression (3.19) formulates explicitly the connection between the evanescent wave modes and the high frequency components of the profile  $f$ . It indicates that a high spatial frequency mode of the scattered field  $\hat{u}(\kappa, d)$  carries high spatial frequency information (fine features) of  $f$  to be reconstructed.*

**Remark 2.2.** *If  $\frac{f}{\lambda} \ll 1$  and the modulus of its derivative  $|f'| \ll 1$ , then (3.19) is reduced automatically to the linear model discussed in [29].*

Now we distinguish the far-field and the near-field cases based on (3.19). When the spatial frequency  $|\kappa| > k$ ,  $e^{ik_2(\kappa)d}$  decreases exponentially with respect to the distance  $d$  and its value vanishes when  $d$  exceeds one wavelength (see Figure 2). Thus in the far-field regime ( $d \gg \lambda$ ),  $\hat{u}(\kappa, d) \approx 0$  for  $|\kappa| > k$ , i.e., the high spatial frequency information of  $f$  is lost in the far-field measurement. In the context of imaging, this

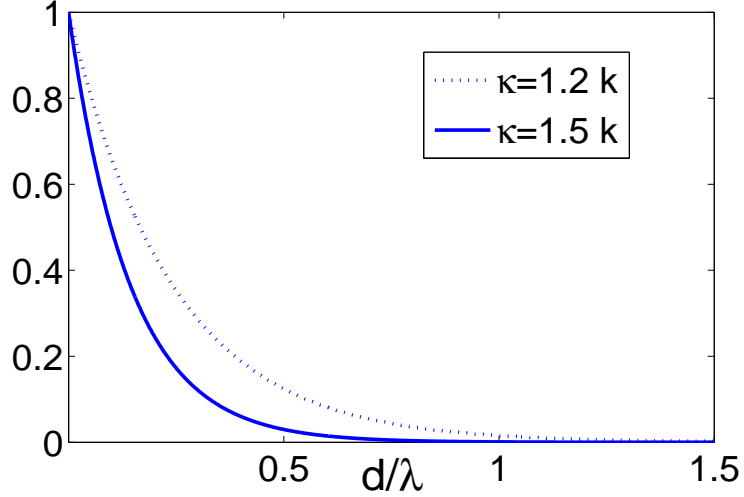


Figure 3.2:  $e^{ik_2(\kappa)d}$  for  $d \in (0, 1.5\lambda)$  when the spatial frequency  $\kappa = 1.2k$  and  $1.5k$  respectively .

implies that it is impossible to recover  $f$  with very high resolution when any noise is present. However, in the near-field regime with  $d < \lambda$ ,  $e^{ik_2(\kappa)d}$  is not close to 0 and the exponentially decayed modes are still significant in the scattered field. Therefore, the higher spatial frequency components of  $f$  can still be retrieved by inverting the evanescent modes of the scattered field.

### 3.3 Near-field Imaging

#### 3.3.1 Inversion Method

Assume that the measurement  $u(\cdot, d)$  is polluted with some additive noise  $n(x_1)$ , which takes the following form

$$n(x_1) = \sigma \cdot \text{rand}(x_1) \cdot u(x_1, d).$$

$\sigma$  is the noise level, and  $\text{rand}(x_1)$  is a uniformly distributed random variable in  $[-1, 1]$  for each  $x_1 \in \mathbb{R}$ . Moreover,  $\text{rand}(x_1)$  is mutually independent for different values of  $x_1$ .

Based on the previous analysis, we present a reconstruction method. From (3.19), we introduce the pseudo-inverse operator  $\mathbf{I}_d$  as follows:

$$\mathbf{I}_d(\kappa) = \begin{cases} e^{-ik_2(\kappa)d} & |\kappa| \leq k_c, \\ 0 & |\kappa| > k_c, \end{cases} \quad (3.20)$$

where  $\mathbf{I}_d(\kappa)$  is a cut-off regularized operator, and  $k_c$  is a regularization parameter.

In the far-field case, as we discuss in the previous section, only the propagating modes can be used for imaging if noise is present, thus the cutoff frequency  $k_c = k$ . In the near-field regime, the bandwidth of the spatial frequency is expanded beyond the wavenumber  $k$  by taking account of the evanescent waves. Note that  $e^{-ik_2(\kappa)d}$  is an exponentially increasing function with respect to  $|\kappa|$  when  $|\kappa| > k$ . Hence, the noise may be exponentially amplified for large  $|\kappa|$ . For fixed distance  $d$ , the cutoff frequency  $k_c$  depends on the noise level (or signal-to-noise ratio). Here, following [29], we choose  $k_c$  in such a way that

$$e^{ik_2(k_c)d} = e^{-\sqrt{k_c^2 - k^2} d} = \sigma. \quad (3.21)$$

That is, the spatial frequency with the transfer function  $e^{ik_2(\kappa)d}$  below the noise level  $\sigma$  is cut off. More explicitly,

$$k_c = \left( k^2 + \left( \frac{\log \frac{1}{\sigma}}{d} \right)^2 \right)^{1/2}. \quad (3.22)$$

In view of (3.21) or (3.22), the pseudo-inverse (3.20) offers a regularization strategy

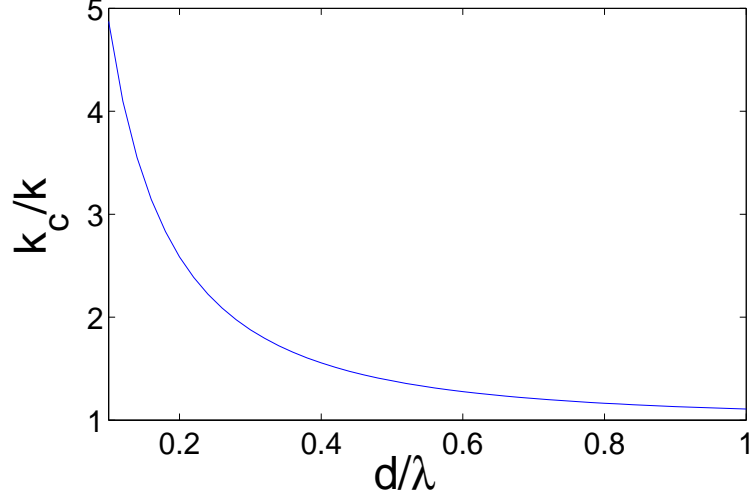


Figure 3.3:  $k_c/k$  versus the distance varying from  $\lambda/10$  to  $\lambda$ .

for the inverse problem. We plot the function  $k_c/k$  for various distance  $d$  in Figure 3 at 5% noise level. It is easily seen that at the fixed noise level, the cutoff frequency  $k_c \gg k$  when  $d < \lambda$ , i.e., the bandwidth of the spatial frequency in the near field is much larger than in the far field. This guarantees better resolution for the final reconstruction in the near-field regime, since the higher spatial frequency components of  $f$  are recovered.

Denote

$$\hat{h}(\kappa) = \mathbf{I}_d(\kappa)\hat{u}(\kappa, d). \quad (3.23)$$

To compute  $h$ , the FFT may be applied to compute the inverse Fourier transform, where  $h$  is an approximation of  $f\varphi$ . To reconstruct  $f$  from  $h$ , we need to take into account of the boundary data on  $\Gamma$ , which turns out to be a (well-posed) nonlinear problem.

We next introduce some notations for representing the surface displacement  $f$ .

Denote by  $C^{0,1}(\bar{\gamma})$  the set of Lipschitz continuous functions on  $\bar{\gamma}$ . Introduce the Banach space  $C_0^{0,1}(\bar{\gamma}) := \{f \mid f \in C^{0,1}(\bar{\gamma}), f = 0 \text{ on } \partial\gamma\}$  with the usual norm

$$\|f\|_{0,1} = \|f\|_{\infty} + \sup_{x_1, y_1 \in \gamma, x_1 \neq y_1} \frac{|f(x_1) - f(y_1)|}{|x_1 - y_1|}.$$

For a fixed small number  $\delta$ , we define

$$\gamma_{\delta} := \{x_1 \in \gamma \mid \text{dist}(x_1, \partial\gamma) < \delta\}.$$

For  $x_1 \in \gamma_{\delta}$ , let  $x_b \in \partial\gamma$  such that  $|x_1 - x_b| = \text{dist}(x_1, \partial\gamma)$ . Assume that  $\{x_1^0, x_1^1, x_1^2 \cdots x_1^N\}$  is a set of grid points defined on  $\bar{\gamma}$ . We represent  $f$  by a piecewise linear function, where

$f$  is linear on  $[x_1^{j-1}, x_1^j]$  for  $j = 1, 2, \dots, N$ , and is continuous on  $\bar{\gamma}$  globally.

Moreover, it is strictly greater than 0 for the interior grid points  $x_1^1, x_1^2 \cdots x_1^{N-1}$ , and is 0 on the boundary  $x_1^0, x_1^N$ . We denote the set of all such functions by  $\mathcal{P}_1$ . It is clear that  $\mathcal{P}_1$  is a subset of  $\tilde{C}_0^{0,1}(\bar{\gamma})$ , which is defined as follows:

$$\begin{aligned} \tilde{C}_0^{0,1}(\bar{\gamma}) := \{f \in C_0^{0,1}(\bar{\gamma}) \mid f(x_1) > 0 \text{ for } x_1 \in \gamma; \exists \epsilon, \delta > 0, \text{ s.t. } f(x_1) \geq \\ \epsilon |x_1 - x_b| \text{ for } x_1 \in \gamma_{\delta}\}. \end{aligned}$$

For fixed grid points  $\{x_1^0, x_1^1, x_1^2 \cdots x_1^N\}$ ,  $\delta = \min\{|x_1^1 - x_1^0|, |x_1^N - x_1^{N-1}|\}$ ,  $\epsilon = \min\left\{\frac{f(x_1^1)}{|x_1^1 - x_1^0|}, \frac{f(x_1^{N-1})}{|x_1^N - x_1^{N-1}|}\right\}$ . On the other hand,  $\tilde{C}_0^{0,1}(\bar{\gamma})$  is an open subset of  $C_0^{0,1}(\bar{\gamma})$ .

We rewrite the integral operator (3.12) on  $\bar{\gamma}$  by introducing the operator  $\tilde{K}_f$  defined as

$$(\tilde{K}_f \varphi)(x_1) := \int_{\bar{\gamma}} G(x_1 - y_1; f(x_1), f(y_1)) \varphi(y_1) dy_1, \quad x_1 \in \bar{\gamma}, \quad (3.24)$$

where  $\varphi = \psi \sqrt{1 + |f'|^2}$ . The kernel of the integral operator  $\tilde{K}_f$  has explicit dependence on  $f$ . Here we adopt the subscript for  $\tilde{K}_f$  to emphasize its dependence on  $f$ . Similarly, define  $\tilde{g}_f(x_1) := g(x_1, f(x_1))$ , where  $g = -(u^i + u^r)|_{\bar{\Gamma}}$  is the boundary data.

A natural way of separating  $f$  from  $h$  computed in (3.23) is to minimize the functional

$$\min_{f \in \mathcal{P}_1} \left( \left\| \tilde{K} f \varphi - \tilde{g}_f \right\|_{L^2(\gamma)} + \|f \varphi - h\|_{L^2(\gamma)} \right). \quad (3.25)$$

However, this minimization problem is difficult to solve in practice, since  $f$  and  $\varphi$  are both unknowns. One alternative is to solve

$$\min_{f \in \mathcal{P}_1} \|f \varphi - h\|_{L^2(\gamma)} \quad \text{subject to } \tilde{K} f \varphi = \tilde{g}_f.$$

It should be pointed out that in general  $\varphi$  is not Fréchet differentiable with respect to  $f$  since the operator  $\tilde{K} f$  is compact. Therefore, existing numerical methods such as Newton's method can not be applied directly.

We introduce a new function  $h_0$  such that  $h_0$  is Lipschitz continuous on  $\bar{\gamma}$ , moreover

$$h_0(x_1) = \begin{cases} h(x_1) & x_1 \in \gamma \setminus \gamma_\delta, \text{ for sufficiently small } \delta; \\ 0 & x_1 \in \partial\gamma. \end{cases} \quad (3.26)$$

By choosing a small  $\delta$  (usually the length of two neighboring grid points),  $\|h_0 - h\|_{L^2(\gamma)}$  is small. In practice,  $h_0$  may be chosen as the following piecewise linear function:

$$h_0(x_1^j) = \begin{cases} h(x_1^j) & j = 1, 2, \dots, N-1; \\ 0 & j = 0, N. \end{cases}$$

Now we match the data on the boundary by solving the minimization problem with a constraint:

$$\min_{f \in \mathcal{P}_1} \left\| \tilde{K} f \varphi - \tilde{g}_f \right\|_{L^2(\gamma)} \quad \text{where } \varphi \in C(\bar{\gamma}) \text{ satisfies } f \varphi = h_0. \quad (3.27)$$

**Remark 3.1.** *The minimization problem (3.27) is a special case of (3.25). By letting  $f \varphi = h_0$ , (3.25) becomes*

$$\min \left\| \tilde{K}_f \varphi - \tilde{g}_f \right\|_{L^2(\gamma)} + \|h_0 - h\|_{L^2(\gamma)},$$

and  $\|h_0 - h\|_{L^2(\gamma)}$  is small by the definition of  $h_0$ .

**Remark 3.2.** For  $f \in \mathcal{P}_1 \subset \tilde{C}_0^{0,1}(\bar{\gamma})$ , the function  $\varphi \in C(\bar{\gamma})$  that satisfies  $f\varphi = h_0$  is well and uniquely defined. Moreover

$$\|\varphi\|_\infty \leq \left( \frac{1}{\min_{x_1 \in \gamma \setminus \gamma_\delta} f(x_1)} + 1/\epsilon \right) \|h_0\|_{0,1}.$$

The problem (3.27) can be solved by Newton's method. Since  $(\frac{f}{\lambda})^2 \ll 1$ , the iteration is expected to converge fast to the real solution, which is confirmed by our numerical examples. To linearize the problem, we require the mapping  $F(f) := \tilde{K}_f \varphi - \tilde{g}_f$  be Fréchet differentiable with respect to  $f \in \mathcal{P}_1$ .

### 3.3.2 Fréchet Differentiability of the Nonlinear Operator

Here and thereafter,  $M$  and  $\tilde{M}$  stand for some generic positive constants, whose values may vary from step to step but should be clear from the contexts. Let  $\mathcal{L}(C(\bar{\gamma}), C(\bar{\gamma}))$  be the set of all bounded linear operators that map the functional space  $C(\bar{\gamma})$  to itself.

**Lemma 3.3.1.** *If  $f \in \tilde{C}_0^{0,1}(\bar{\gamma}) \subset C_0^{0,1}(\bar{\gamma})$ , then the mapping  $f \rightarrow \tilde{K}_f$  is Fréchet differentiable from  $C_0^{0,1}(\bar{\gamma})$  to  $\mathcal{L}(C(\bar{\gamma}), C(\bar{\gamma}))$ . Moreover, the Fréchet derivative is the linear mapping  $\delta_f \rightarrow (\tilde{K}_f)'(\delta_f)$  for  $\delta_f \in C_0^{0,1}(\bar{\gamma})$ , where  $(\tilde{K}_f)'(\delta_f) \in \mathcal{L}(C(\bar{\gamma}), C(\bar{\gamma}))$  is defined as*

$$\begin{aligned} [(\tilde{K}_f)'(\delta_f)]\varphi(x_1) &= \int_{\bar{\gamma}} \left[ \frac{\partial \tilde{\Phi}(x_1 - y_1, f(x_1) - f(y_1))}{\partial x_2} (\delta_f(x_1) - \delta_f(y_1)) \right. \\ &\quad \left. - \frac{\partial \tilde{\Phi}(x_1 - y_1, f(x_1) + f(y_1))}{\partial x_2} (\delta_f(x_1) + \delta_f(y_1)) \right] \varphi(y_1) dy_1 \end{aligned}$$

for  $\varphi \in C(\bar{\gamma})$ .

**Proof.** It is clear that the mapping  $\delta_f \rightarrow (\tilde{K}_f)'(\delta_f)$  is linear.

*Step1: the mapping  $\delta_f \rightarrow (\tilde{K}_f)'(\delta_f)$  is bounded.*

Denote

$$r_1 = \sqrt{(x_1 - y_1)^2 + (f(x_1) - f(y_1))^2}, \quad r_2 = \sqrt{(x_1 - y_1)^2 + (f(x_1) + f(y_1))^2}.$$

We first estimate the first part:

$$\begin{aligned} \left| \frac{\partial \tilde{\Phi}(x_1 - y_1, f(x_1) - f(y_1))}{\partial x_2} \right| &= \left| \frac{ik}{4} \left( H_0^{(1)}(kr_1) \right)' \frac{f(x_1) - f(y_1)}{r_1} \right| \\ &\leq \frac{k}{4} \left| \left( H_0^{(1)}(kr_1) \right)' \right|. \end{aligned}$$

For a small fixed constant  $\tau_0$ , if  $|y_1 - x_1| \geq \tau_0$  (away from the singularity), then

$$\left| \left( H_0^{(1)}(kr_1) \right)' \right| \leq \tilde{M}.$$

It follows that

$$\begin{aligned} &\left| \int_{\bar{\gamma} \setminus \{|y_1 - x_1| < \tau_0\}} \frac{\partial \tilde{\Phi}(x_1 - y_1, f(x_1) - f(y_1))}{\partial x_2} (\delta_f(x_1) - \delta_f(y_1)) \varphi(y_1) dy_1 \right| \\ &\leq M \|\delta_f\|_{0,1} \|\varphi\|_{\infty}. \end{aligned}$$

On the other hand, if  $|y_1 - x_1| < \tau_0$ ,  $\left| \left( H_0^{(1)}(kr_1) \right)' \right| \sim O\left(\frac{1}{r_1}\right)$  for  $\tau_0$  sufficiently small. We have

$$\begin{aligned} &\left| \int_{\{|y_1 - x_1| < \tau_0\}} \frac{\partial \tilde{\Phi}(x_1 - y_1, f(x_1) - f(y_1))}{\partial x_2} (\delta_f(x_1) - \delta_f(y_1)) \varphi(y_1) dy_1 \right| \\ &\leq \int_{\{|y_1 - x_1| < \tau_0\}} \frac{M}{r_1} |x_1 - y_1| dy_1 \|\delta_f\|_{0,1} \|\varphi\|_{\infty} \leq M \|\delta_f\|_{0,1} \|\varphi\|_{\infty}. \end{aligned}$$

For the second part,

$$\begin{aligned}
& \int_{\bar{\gamma}} \frac{\partial \tilde{\Phi}(x_1 - y_1, f(x_1) + f(y_1))}{\partial x_2} (\delta_f(x_1) + \delta_f(y_1)) \varphi(y_1) dy_1 \\
&= \int_{\bar{\gamma}} \frac{\partial \tilde{\Phi}(x_1 - y_1, f(x_1) + f(y_1))}{\partial x_2} [\delta_f(y_1) - \delta_f(x_1)] \varphi(y_1) dy_1 \\
&\quad + 2 \int_{\bar{\gamma}} \frac{\partial \tilde{\Phi}(x_1 - y_1, f(x_1) + f(y_1))}{\partial x_2} \varphi(y_1) dy_1 \delta_f(x_1) \\
&=: \mathcal{A}_1 + \mathcal{A}_2
\end{aligned}$$

From the estimate of the first term, the following inequality also holds:

$$|\mathcal{A}_1| \leq M \|\delta_f\|_{0,1} \|\varphi\|_{\infty}.$$

For  $x_1 \in \gamma \setminus \gamma_{\delta}$ ,

$$|\mathcal{A}_2| \leq M_{\delta} \|\delta_f\|_{0,1} \|\varphi\|_{\infty}, \quad \text{where } M_{\delta} = \frac{k}{2} \min_{x_1 \in \gamma \setminus \gamma_{\delta}} \left| \left( H_0^{(1)}(kf(x_1)) \right)' \right|.$$

For  $x_1 \in \gamma_{\delta}$ ,

$$\begin{aligned}
|\mathcal{A}_2| &\leq \frac{k}{2} \left( \int_{\bar{\gamma} \setminus [x_1 - \delta/2, x_1 + \delta/2]} + \int_{[x_1 - \delta/2, x_1 + \delta/2]} \right) \left| \left( H_0^{(1)}(kr_2) \right)' \right| dy_1 \\
&\quad \left| \delta_f(x_1) \right| \|\varphi\|_{\infty} \\
&\leq \tilde{M} \left| \left( H_0^{(1)}\left(\frac{k\delta}{2}\right) \right)' \right| \|\delta_f\|_{0,1} \|\varphi\|_{\infty} \\
&\quad + \tilde{M} \int_{x_1 - \delta/2}^{x_1 + \delta/2} \frac{1}{\sqrt{(y_1 - x_1)^2 + f(x_1)^2}} dy_1 \left| \delta_f(x_1) \right| \|\varphi\|_{\infty} \\
&\leq \tilde{M} \left[ \left| \left( H_0^{(1)}\left(\frac{k\delta}{2}\right) \right)' \right| + \ln 2 - \ln\left(1 - \frac{\delta}{\sqrt{\delta^2 + (\epsilon/2)^2 |x_1 - x_b|^2}}\right) |x_1 - x_b| \right]
\end{aligned}$$

$$\leq \tilde{M} \left[ \left| \left( H_0^{(1)} \left( \frac{k\delta}{2} \right) \right)' \right| + \ln 2 - \ln \left( 1 - \frac{\delta}{\sqrt{\delta^2 + (\epsilon/2)^2 |x_1 - x_b|^2}} \right) |x_1 - x_b| \right] \|\delta_f\|_{0,1} \|\varphi\|_\infty.$$

The last inequality follows from the fact that there exists an  $\epsilon$  such that  $f(x_1) \geq \epsilon |x_1 - x_b|$  for  $x_1 \in \gamma_\delta$ , and  $|\delta_f(x_1)| \leq \|\delta_f\|_{0,1} |x_1 - x_b|$ .

Therefore

$$|\mathcal{A}_2| \leq M(\epsilon, \delta) \|\delta_f\|_{0,1} \|\varphi\|_\infty,$$

where

$$\begin{aligned} M(\epsilon, \delta) &= \tilde{M} \left| \left( H_0^{(1)} \left( \frac{k\delta}{2} \right) \right)' \right| + \tilde{M} \ln 2 \\ &\quad - \tilde{M} \inf_{x_1 \in \gamma_{\delta/2}} \left( \ln \left( 1 - \frac{\delta}{\sqrt{\delta^2 + (\epsilon/2)^2 |x_1 - x_b|^2}} \right) |x_1 - x_b| \right) \end{aligned}$$

is a positive constant.

Therefore

$$\left\| [(\tilde{K}_f)'(\delta_f)]\varphi \right\|_\infty \leq M(\epsilon, \delta, f) \|\delta_f\|_{0,1} \|\varphi\|_\infty$$

for any  $\varphi \in C(\bar{\gamma})$ , i.e.,

$$\left\| (\tilde{K}_f)'(\delta_f) \right\|_{\mathcal{L}(C(\bar{\gamma}), C(\bar{\gamma}))} \leq M(\epsilon, \delta, f) \|\delta_f\|_{0,1}.$$

Step2: An estimate of the remainder term  $\tilde{K}_{f+\delta f} - \tilde{K}_f - (\tilde{K}_f)'(\delta_f)$ .

For any  $\varphi \in C(\bar{\gamma})$ , by Taylor's formula,

$$\begin{aligned}
& [\tilde{K}_{f+\delta f} - \tilde{K}_f - (\tilde{K}_f)'(\delta_f)]\varphi(x_1) \\
= & \int_{\bar{\gamma}} \int_0^1 \frac{\partial^2 \tilde{\Phi}(x_1 - y_1, f(x_1) - f(y_1) + t(\delta_f(x_1) - \delta_f(y_1)))}{\partial x_2^2} dt \\
& [\delta_f(x_1) - \delta_f(y_1)]^2 \varphi(y_1) dy_1 \\
& - \int_{\bar{\gamma}} \int_0^1 \frac{\partial^2 \tilde{\Phi}(x_1 - y_1, f(x_1) + f(y_1) + t(\delta_f(x_1) + \delta_f(y_1)))}{\partial x_2^2} dt \\
& [\delta_f(x_1) + \delta_f(y_1)]^2 \varphi(y_1) dy_1 \\
= & \mathcal{B}_1 + \mathcal{B}_2.
\end{aligned}$$

By a similar argument as in Step 1, we can estimate  $\mathcal{B}_1$ . Assume that  $\|\delta_f\|_{0,1}$  is sufficiently small. For a fixed small constant  $\tau_0$ , if  $|y_1 - x_1| \geq \tau_0$  (away from singularity), then

$$\begin{aligned}
& \int_{\bar{\gamma} \setminus \{|y_1 - x_1| < \tau_0\}} \int_0^1 \left| \frac{\partial^2 \tilde{\Phi}(x_1 - y_1, f(x_1) - f(y_1) + t(\delta_f(x_1) - \delta_f(y_1)))}{\partial x_2^2} \right| dt \\
& [\delta_f(x_1) - \delta_f(y_1)]^2 |\varphi(y_1)| dy_1 \leq M \|\delta_f\|_{0,1}^2 \|\varphi\|_\infty.
\end{aligned}$$

If  $|y_1 - x_1| < \tau_0$ ,  $\left| \frac{\partial^2 \tilde{\Phi}}{\partial x_2^2} \right| \sim O\left(\frac{1}{r_1^2}\right)$  for  $\tau_0$  sufficiently small. Thus

$$\begin{aligned}
& \int_{\{|y_1 - x_1| < \tau_0\}} \int_0^1 \left| \frac{\partial^2 \tilde{\Phi}(x_1 - y_1, f(x_1) - f(y_1) + t(\delta_f(x_1) - \delta_f(y_1)))}{\partial x_2^2} \right| dt \\
& [\delta_f(x_1) - \delta_f(y_1)]^2 |\varphi(y_1)| dy_1 \leq \int_{\{|y_1 - x_1| < \tau_0\}} \frac{M}{r_1^2} |x_1 - y_1|^2 dy_1 \|\delta_f\|_{0,1}^2 \|\varphi\|_\infty \\
& \leq M \|\delta_f\|_{0,1}^2 \|\varphi\|_\infty.
\end{aligned}$$

Next, the term  $\mathcal{B}_2$  can also be split into two parts  $\mathcal{B}_2^1$  and  $\mathcal{B}_2^2$ :

$$\mathcal{B}_2^1 = \int_{\bar{\gamma}} \int_0^1 \frac{\partial^2 \tilde{\Phi}(x_1 - y_1, f(x_1) + f(y_1) + t(\delta_f(x_1) + \delta_f(y_1)))}{\partial x_2^2} dt \\ [\delta_f(x_1) - \delta_f(y_1)]^2 \varphi(y_1) dy_1$$

and

$$\mathcal{B}_2^2 = 4 \int_{\bar{\gamma}} \int_0^1 \frac{\partial^2 \tilde{\Phi}(x_1 - y_1, f(x_1) + f(y_1) + t(\delta_f(x_1) + \delta_f(y_1)))}{\partial x_2^2} dt \\ [\delta_f(x_1) \delta_f(y_1)] \varphi(y_1) dy_1.$$

It suffices to estimate  $\mathcal{B}_2^2$ .

For  $x_1 \in \gamma \setminus \gamma_{\frac{\delta}{2}}$ ,

$$|\mathcal{B}_2^2| \leq M_{\delta} \|\delta_f\|_{0,1}^2 \|\varphi\|_{\infty},$$

where

$$M_{\delta} = \min_{x_1 \in \gamma \setminus \gamma_{\frac{\delta}{2}}} k^2 \left| \left( H_0^{(1)} \left( \frac{2k}{f(x_1)} \right) \right)'' \right| + \frac{2k}{f(x_1)} \left| \left( H_0^{(1)} \left( \frac{2k}{f(x_1)} \right) \right)' \right|$$

if  $\|\delta_f\|_{0,1}$  is sufficiently small.

For  $x_1 \in \gamma_{\frac{\delta}{2}}$ ,

$$|\mathcal{B}_2^2| \leq \left( \int_{\bar{\gamma} \setminus [x_1 - \delta/2, x_1 + \delta/2]} + \int_{[x_1 - \delta/2, x_1 + \delta/2]} \right) \left( \int_0^1 \left| \frac{\partial^2 \tilde{\Phi}}{\partial x_2^2} \right| dt \right) dy_1 \\ |\delta_f(x_1)| \|\delta_f\|_{0,1} \|\varphi\|_{\infty}$$

$$\begin{aligned}
&\leq \tilde{M}_\delta \left\| \delta f \right\|_{0,1}^2 \|\varphi\|_\infty + \tilde{M} \int_{x_1-\delta/2}^{x_1+\delta/2} \frac{1}{(y_1-x_1)^2 + (\epsilon/2)^2 |x_1-x_b|^2} dy_1 \\
&\quad \left| \delta f(x_1) \right| \left\| \delta f \right\|_{0,1} \|\varphi\|_\infty \\
&\leq \tilde{M}_\delta \left\| \delta f \right\|_{0,1}^2 \|\varphi\|_\infty + \frac{\tilde{M}}{\epsilon/2 |x_1-x_b|} \left| \delta f(x_1) \right| \left\| \delta f \right\|_{0,1} \|\varphi\|_\infty . \\
&\leq M(\epsilon, \delta) \left\| \delta f \right\|_{0,1}^2 \|\varphi\|_\infty .
\end{aligned}$$

Therefore

$$\left\| \tilde{K}_{f+\delta f} - \tilde{K}_f - (\tilde{K}_f)'(\delta f) \right\|_{\mathcal{L}(C(\bar{\gamma}), C(\bar{\gamma}))} = O\left(\left\| \delta f \right\|_{0,1}^2\right),$$

for sufficiently small  $\left\| \delta f \right\|_{0,1}$ , which completes the proof.  $\square$

Let  $h_0 \in C_0^{0,1}(\bar{\gamma})$  be defined as in (3.26). For  $f \in \mathcal{P}_1 \subset \tilde{C}_0^{0,1}(\bar{\gamma})$ , let  $\varphi \in C(\bar{\gamma})$  satisfy  $f\varphi = h_0$ . The following lemma concerns the Fréchet derivative of the mapping  $f \rightarrow \varphi$  ( $C_0^{0,1}(\bar{\gamma}) \rightarrow C(\bar{\gamma})$ ).

**Lemma 3.3.2.** *If  $f \in \tilde{C}_0^{0,1}(\bar{\gamma}) \subset C_0^{0,1}(\bar{\gamma})$ , then the mapping  $f \rightarrow \varphi$  defined as the above is Fréchet differentiable from  $C_0^{0,1}(\bar{\gamma})$  to  $C(\bar{\gamma})$ . Moreover, its Fréchet derivative is the linear mapping  $\delta f \rightarrow \varphi'$  for  $\delta f \in C_0^{0,1}(\bar{\gamma})$ , where  $\varphi' \in C(\bar{\gamma})$  and*

$$\varphi'(x_1) = -\frac{\varphi(x_1)}{f(x_1)} \delta f(x_1) \text{ for } x_1 \in \gamma.$$

**Proof.** It is easy to show that

$$\left| \varphi'(x_1) \right| \leq \left(M_\delta + \frac{1}{\epsilon}\right) \|\varphi\|_\infty \left\| \delta f \right\|_{0,1} \quad \text{for } x_1 \in \gamma,$$

where  $M_\delta = \min_{x_1 \in \gamma \setminus \gamma_\delta} \frac{1}{f(x_1)}$  is a constant. Therefore

$$\left\| \varphi' \right\|_\infty \leq \left(M_\delta + \frac{1}{\epsilon}\right) \|\varphi\|_\infty \left\| \delta f \right\|_{0,1}$$

and the mapping  $\delta f \rightarrow \varphi'$  is bounded from  $C_0^{0,1}(\bar{\gamma}) \rightarrow C(\bar{\gamma})$ .

For a perturbation of  $f$  with  $\delta_f \in C_0^{0,1}(\bar{\gamma})$ , a perturbation of  $\varphi$  satisfies

$$(\varphi + \delta\varphi)(f + \delta f) = h_0.$$

If  $\|\delta_f\|_{0,1}$  is sufficiently small, for  $x_1 \in \gamma$ , the following estimate for the high order term holds:

$$\begin{aligned} & \left| (\varphi + \delta\varphi)(x_1) - \varphi(x_1) - \varphi'(x_1) \right| \\ &= \frac{1}{\left| (f(x_1) + \delta f(x_1))f(x_1) \right|} |\varphi(x_1)| \left| \delta f(x_1) \right| \\ &\leq \frac{1}{2} \left( M_\delta^2 + \frac{1}{\epsilon^2} \right) \|\varphi\|_\infty \|\delta_f\|_{0,1}^2. \end{aligned}$$

Thus

$$\left\| (\varphi + \delta\varphi) - \varphi - \varphi' \right\|_\infty = O\left( \|\delta_f\|_{0,1}^2 \right),$$

for sufficiently small  $\|\delta_f\|_{0,1}$ . □

By Taylor's expansion, it is easily seen that the mapping  $f \rightarrow \tilde{g}_f (:= g(x_1, f(x_1)))$  is also Fréchet differentiable from  $C_0^{0,1}(\bar{\gamma})$  to  $C(\bar{\gamma})$ . We denote its Fréchet derivative as the mapping  $\delta f \rightarrow \tilde{g}'_f$ . Combining Lemma 3.3.1 and Lemma 3.3.2 and using the product rule, we have the following theorem:

**Theorem 3.3.3.** *If  $f \in \tilde{C}_0^{0,1}(\bar{\gamma}) \subset C_0^{0,1}(\bar{\gamma})$ ,  $F(f) := \tilde{K}_f \varphi - \tilde{g}_f$  is Fréchet differentiable from  $C_0^{0,1}(\bar{\gamma})$  to  $C(\bar{\gamma})$ . Moreover, the Fréchet derivative maps  $\delta f$  to  $DF(\delta f) = [(\tilde{K})'_f(\delta f)]\varphi + \tilde{K}_f(\varphi') - \tilde{g}'_f$ .*

## 3.4 Numerical Examples

First, let us consider the solution of the forward scattering problem. By Proposition 3.2.3, if  $k^2$  is not an eigenvalue of  $-\Delta$  in  $\tilde{D}$ , to solve the forward scattering problem (4.1)-(4.3) efficiently in our numerical simulation, we can firstly solve the integral

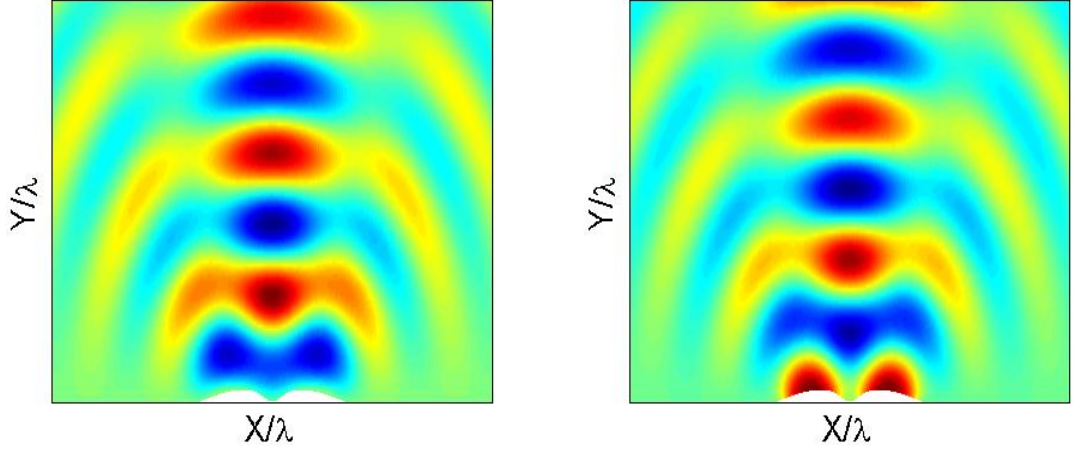


Figure 3.4: Real part (left) and the imaginary part (right) of the scattered field.

equation  $K\psi = g$  and substitute  $\psi$  into (3.7). If  $k^2$  is an eigenvalue, then the forward scattering problem can be solved by introducing the artificial boundary (e.g. half circle) and solving the problem in a bounded domain. Since our focus is on inverse problem, without loss of generality, we assume that  $k^2$  is not an eigenvalue in our numerical examples.

In the following examples, an incident wave  $u^i = e^{ikq \cdot x}/100^2$  with normal incident direction impinges on the obstacle. The wavenumber  $k = 100$ ,  $\lambda \approx 6.28$  cm,  $q = (0, -1)^T$ . In all the figures, the plots are rescaled with respect to the wavelength  $\lambda$ .

**Example 4.1.** The real surface displacement is represented by two bumps, each one with the size of order  $\lambda$ . The two bumps are close to each other, and separated with distance  $\lambda/10$ . The scattered field in the region  $[-3\lambda, 3\lambda] \times [0, 3\lambda]$  is plotted in Figure 3.4. Data are collected above the obstacle with distance  $d = \lambda/5$  (near-field). We also assume that 5% noise is added to the simulation data. It follows from

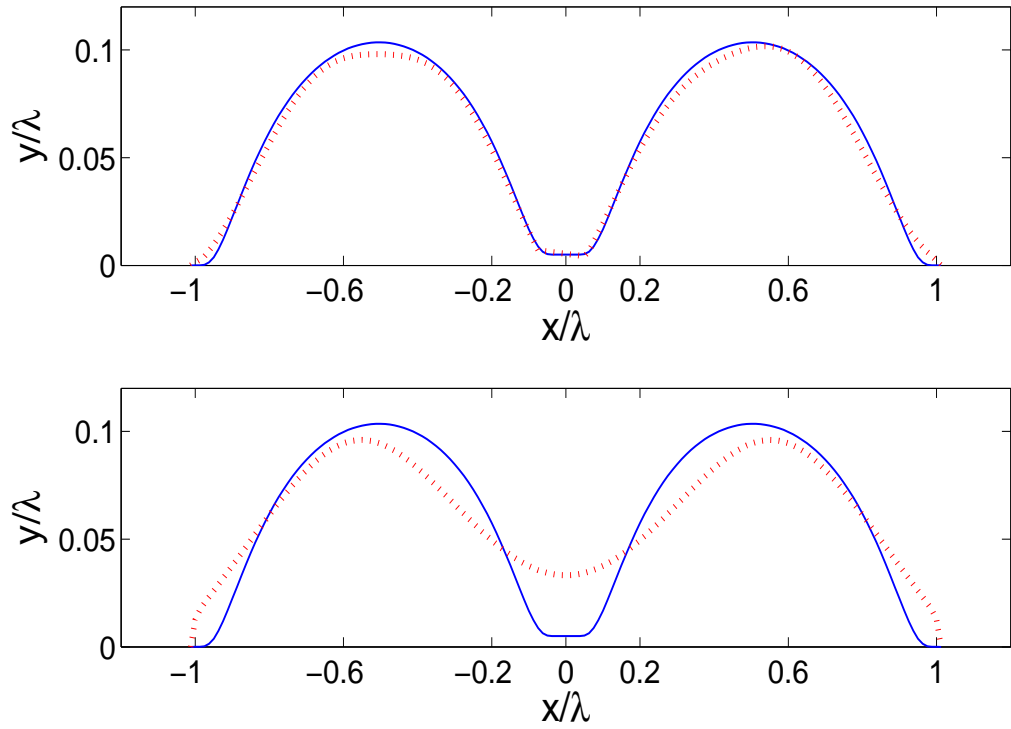


Figure 3.5: Near-field (top) and far-field (bottom) images. The solid line represents the real image, and the dotted line is the reconstruction.

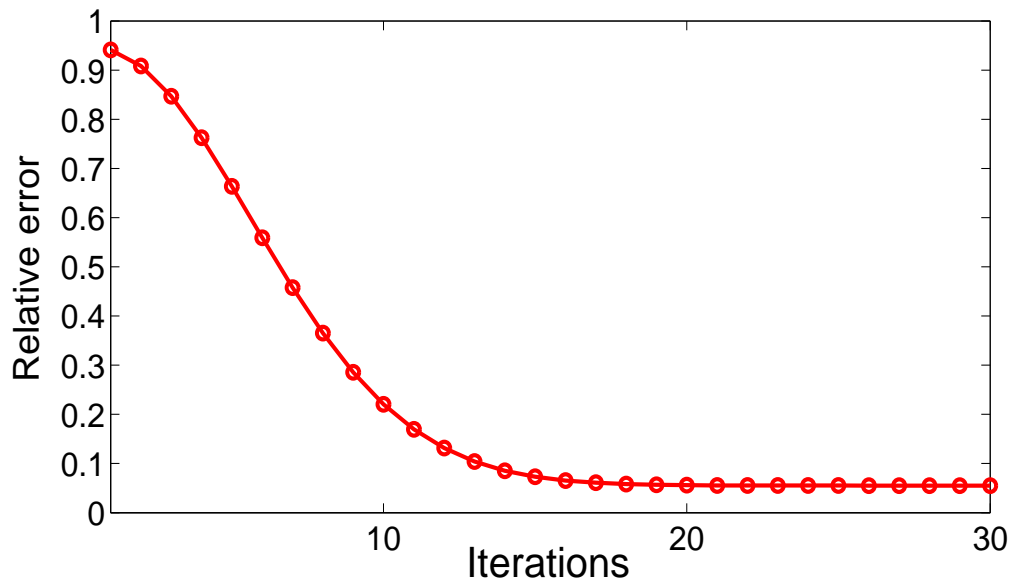


Figure 3.6: Relative error with respect to Newton iterations.

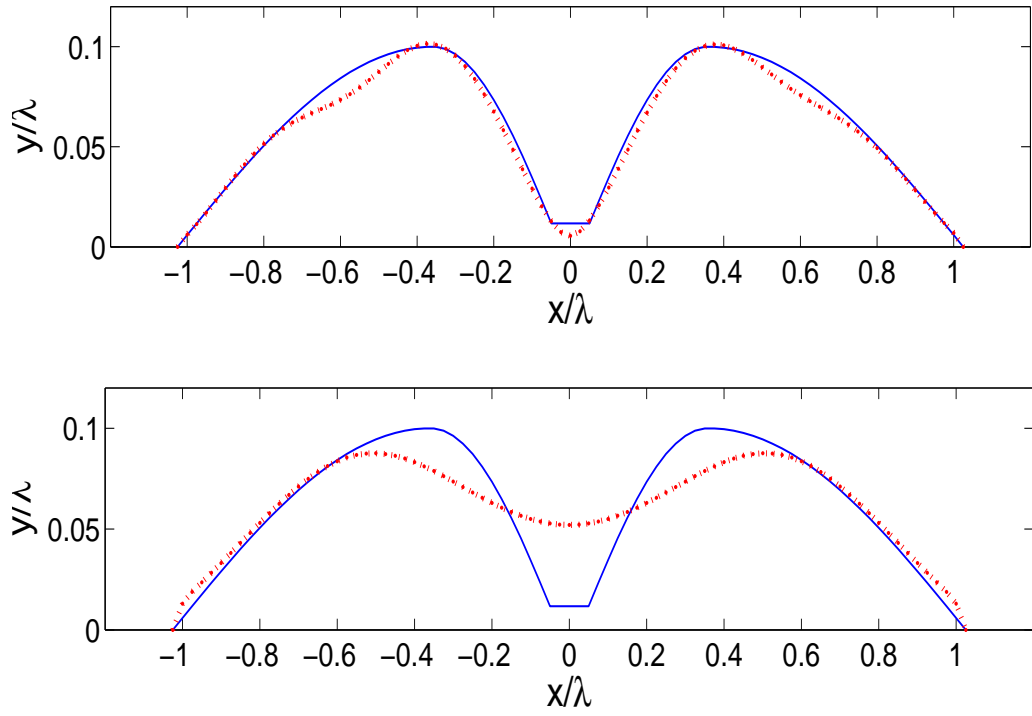


Figure 3.7: Near-field (left) and far-field (right) images. The solid line represents the real image, and the dotted line is the reconstruction.

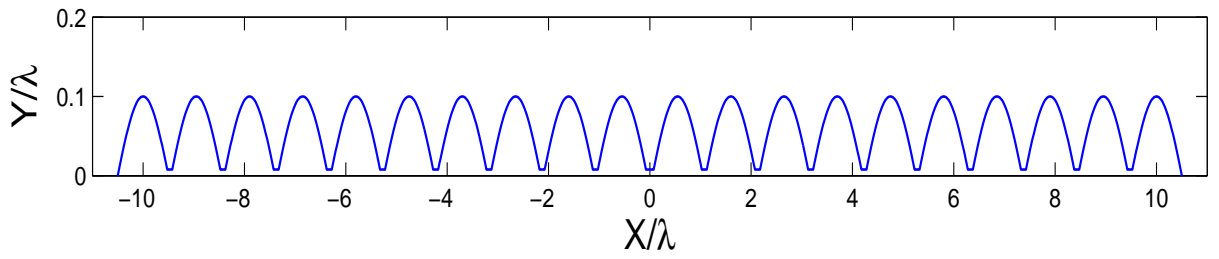


Figure 3.8: Real profile, the distance between neighboring bumps is  $\lambda/10$ .

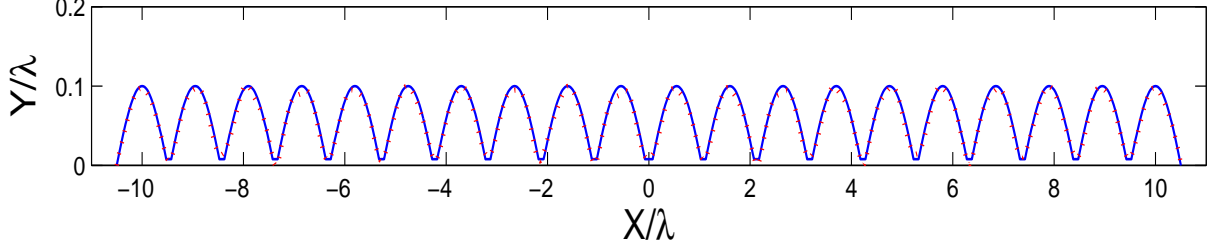


Figure 3.9: Comparison of the reconstruction (dotted line) with the real profile (solid line) for the near-field case.

(3.22) that  $k_c \approx 2.6k$ . The near-field image  $f_n$  and the real image  $f$  are plotted in Figure 3.5 (left). Though two bumps are close to each other ( $\lambda/10$ ), they are clear distinguishable. Therefore, super-resolution is achieved with near-field measurements. To confirm the convergence of Newton's method for solving the minimization problem (3.27), the relative error is shown with respect to the iteration number in Figure 3.6. Here the relative error is defined as

$$\frac{\left(\sum_{j=0}^N |f(x_1^j) - f_n(x_1^j)|^2\right)^{1/2}}{\left(\sum_{j=0}^N f(x_1^j)^2\right)^{1/2}}.$$

The reconstruction converges fast, which leads to the real surface displacement after the first 20 iterations.

To compare with the far-field image, we collect the data again with  $d = 5\lambda$  and 5% noise. It is obvious that  $k_c = k$  in the far-field case. The image  $f_n$  is shown in Figure 3.5 (right). It is clear that the two bumps can not be distinguished, which is due to the fact that the high spatial frequency information of the surface displacement is lost.

**Example 4.2** We consider a non-smooth profile in this example. Two bumps are separated with distance  $\lambda/10$ . The measurement is polluted with 5% noise. Figure 3.7 is the reconstructed near-field and far-field images when  $d = \lambda/5$  and  $5\lambda$  respec-

tively. Super-resolution is also achieved via near-field imaging. On the other hand, it is also observed that the accuracy of the reconstruction is deteriorated when data is collected at far field.

**Example 4.3** The real surface displacement is a long periodic structure (see Figure 3.8). Each period is a bump with size of order  $\lambda$ , and two neighboring bumps are separated with distance  $\lambda/10$ . The measurement distance  $d$  again is  $\lambda/5$ , where 5% noise is added to the simulation data. We compare the near-field image and the real image in Figure 3.9. The periodic structure is also accurately reconstructed with super-resolution.

## 3.5 Discussions

The proposed numerical method in the near-field regime, which recovers high spatial frequency modes of the surface displacement by taking account of the evanescent modes, yields super-resolution for the reconstructed image.

Numerically, the Newton iteration for the minimization problem (3.27) converges fast to the real solution. However, no rigorous theoretical convergence analysis is presently available. Another issue is denoising in the near-field regime. Noise will be exponentially amplified in near-field regime. The cutoff wavenumber  $k_C$ , which is the critical parameter for the resolution of the reconstructed image, strongly depends on the noise level. A denosing technique based on the broadband signal has recently been proposed in [29] for the linearized model. For the nonlinear imaging, the problem becomes much more challenging and is completely open.

To reconstruct more general local surface displacement (without assumption  $(\frac{f}{\lambda})^2 \ll 1$ ), we propose to use multiple frequency data. This is discussed fully in the next Chapter.

# Chapter 4

## Imaging with Multiple Frequency Data

### 4.1 Introduction

#### 4.1.1 Problem Formulations

We consider the very general case without specific restriction on the surface displacement in this Chapter. Figure 4.1 is the schematic setup of the scattering problem and data collection. As in Chapter 3, we let  $x = (x_1, x_2)$ , and  $f(x_1)$  be a function defined on the real line  $\mathbb{R}$  with compact support  $\gamma$ . The curve  $\partial D := \{ x \mid x_1 \in \mathbb{R}, x_2 = f(x_1) \}$  represents the boundary of the whole obstacle on which the electromagnetic wave impinges, and the domain above  $\partial D$  is denoted as  $D$ .

Let  $R$  be some positive constant such that  $\gamma \subset\subset (-R, R)$  and  $\Gamma := \{ x \mid x_1 \in (-R, R), x_2 = f(x_1) \}$  represent the local disturbance. Let  $B_R$  be a disk with radius  $R$  centered at origin.  $\partial B_R^+ := \partial B_R \cap D$  is the half circle above the ground plane, where  $\partial B_R$  is the boundary of the disk  $B_R$ . Without loss of generality, we assume that  $\Gamma$  lies below  $\partial B_R^+$  ( see Figure 4.1). We also denote the domain bounded by

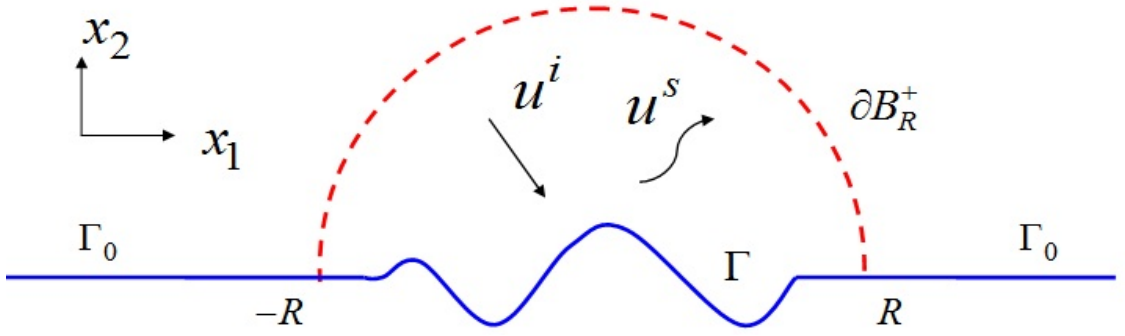


Figure 4.1: Problem geometry.

$\partial B_R^+ \cup \Gamma$  as  $D_R$ .

The mathematical model for the forward scattering problem is the same as in Chapter 3. The total field  $u$  satisfies the Helmholtz equation

$$\Delta u + k^2 u = 0 \quad \text{in } D. \quad (4.1)$$

and vanishes on the boundary:

$$u = 0 \quad \text{on } \partial D. \quad (4.2)$$

In addition, at infinity the scattered field  $u^s$  satisfies the Sommerfeld radiation condition:

$$\lim_{r \rightarrow \infty} \sqrt{r} \left( \frac{\partial u^s}{\partial r} - i k u^s \right) = 0, \quad r = |x|. \quad (4.3)$$

Now we are ready to present the inverse scattering problem. The total field  $u$  is collected on the half circle  $\partial B_R^+$ , and the measurements are assumed to be available for a set of wavenumbers  $\{k_j \mid j = 1, 2, \dots, M; k_j < k_{j+1}\}$ . The inverse problem is to reconstruct the local disturbance  $\Gamma$  from the measured multiple frequency data on  $\partial B_R^+$ .

### 4.1.2 Why Multiple Frequency Data

In the presence of noise, the resolution of the reconstructed image is usually limited by the operating frequency of the electromagnetic wave. When the height of the displacement is small compared to the wavelength, it is already observed in Chapter 3 that a high spatial frequency mode of the scattered wave contains exactly the high spatial frequency information (fine features) of the profile. Theoretical studies also reveal that higher frequency information may yield increased stability (less ill-posedness).

In fact, in our recent paper on a multiple frequency inverse source problem for the Helmholtz equation [12], it is proved that a Hölder type stability estimate may be obtained with sufficiently high wavenumber. In [40], Isakov also proved increased stability for reconstructing the Schrödinger potential from the Dirichlet-to-Neumann map with higher wavenumber. On the other hand, when only single frequency data is available, classical regularized iterative optimization methods such as Newton's method ( see for example [31] ) applied to the inverse scattering problem usually fail to compute the global minimizer. Multiple frequency data overcomes the difficulty of reaching some local minimum. In [7, 8, 9, 22], a stable recursive linearization method is developed for the inverse medium scattering problem with multiple frequency data. The method applies the Born approximation at the lowest frequency to obtain the initial guess of the medium, and sequentially updates at higher frequency until the dominant modes of the medium are essentially recovered. The convergence of the recursive linearization method has been analyzed recently in [13].

## 4.2 Analysis of the Forward Scattering Problem

### 4.2.1 Notations

We begin with some standard notations that will be used throughout this Chapter.

Let

$$\mathcal{H}^1(D_R) := \{ u \mid u \in L^2(D_R), \partial_j u \in L^2(D_R) \}$$

be the standard Sobolev space equipped with the norm

$$\|u\|_{1,D_R} = \|u\|_{0,D_R} + |u|_{1,D_R},$$

where

$$\|u\|_{0,D_R}^2 = \int_{D_R} |u(x)|^2 dx, \quad |u|_{1,D_R}^2 = \sum_{j=1}^2 \int_{D_R} |\partial_j u|^2 dx.$$

Let  $(r, \theta)$  represent the polar coordinates. Define the Sobolev space  $\mathcal{H}^{1/2}(\partial B_R)$  as

$$\mathcal{H}^{1/2}(\partial B_R) := \{ \varphi \in L^2(\partial B_R) \mid \sum_{n=0}^{\infty} \sqrt{1+n^2} \left( |\varphi_n^s|^2 + |\varphi_n^c|^2 \right) < +\infty \},$$

where  $\varphi_n^s$  and  $\varphi_n^c$  are the Fourier coefficients of the function  $\varphi$  on the circle  $\partial B_R$ :

$$\varphi_n^s = \frac{1}{\pi} \int_{-\pi}^{\pi} \varphi(\theta) \sin(n\theta) d\theta \quad (n \geq 0),$$

$$\varphi_0^c = \frac{1}{2\pi} \int_{-\pi}^{\pi} \varphi(\theta) d\theta, \quad \varphi_n^c = \frac{1}{\pi} \int_{-\pi}^{\pi} \varphi(\theta) \cos(n\theta) d\theta \quad (n \geq 1).$$

For a function  $\varphi$  defined on the half circle  $\partial B_R^+$ , it is extended to  $\partial B_R$  by odd reflection:

$$\tilde{\varphi}(\theta) = \begin{cases} \varphi(\theta) & \theta \in (0, \pi), \\ -\varphi(-\theta) & \theta \in (-\pi, 0). \end{cases}$$

Define

$$\tilde{\mathcal{H}}^{1/2}(\partial B_R^+) := \{ \varphi \in \mathcal{H}^{1/2}(\partial B_R^+) \mid \tilde{\varphi} \in \mathcal{H}^{1/2}(\partial B_R), \text{ where } \tilde{\varphi} \text{ is the odd extension of } \varphi \}.$$

Let

$$\varphi_n = \frac{2}{\pi} \int_0^\pi \varphi(\theta) \sin(n\theta) d\theta.$$

Clearly  $\tilde{\varphi}_n^s = \varphi_n$  and  $\tilde{\varphi}_n^c = 0$ . Hence

$$\tilde{\mathcal{H}}^{1/2}(\partial B_R^+) = \{ \varphi \in \mathcal{H}^{1/2}(\partial B_R^+) \mid \sum_{n=1}^{\infty} \sqrt{1+n^2} |\varphi_n|^2 < +\infty \},$$

with the norm

$$\|\varphi\|_{\tilde{\mathcal{H}}^{1/2}(\partial B_R^+)} = \left( \sum_{n=1}^{\infty} \sqrt{1+n^2} |\varphi_n|^2 \right)^{1/2}.$$

## 4.2.2 Dirichlet-to-Neumann Map

We reformulate the forward scattering model (4.1) - (4.3) in the bounded domain  $D_R$  by introducing the Dirichlet-to-Neumann map on  $\partial B_R^+$ . A similar Dirichlet-to-Neumann map is also introduced in [63] for the scattering from an overfilled cavity. In fact, the idea of using pseudo-differential operators to reduce the infinite domain to a bounded domain has been applied to various wave simulation problems. See for example [3, 4, 33].

Let  $\varphi(\theta) = u^s|_{\partial B_R^+}$ . From (4.1) - (4.3), it follows that the scattered field  $u^s$  satisfies

$$\begin{cases} \Delta u^s + k^2 u^s = 0 & \text{in } D \setminus B_R, \\ u^s = \varphi & \text{on } \partial B_R^+, \\ u^s = 0 & \text{on } \Gamma_0, \\ \lim_{r \rightarrow \infty} \sqrt{r} \left( \frac{\partial u^s}{\partial r} - iku^s \right) = 0, \quad r = |x|. \end{cases}$$

The solution of the scattering problem takes the form

$$u^s(r, \theta) = \sum_{n=1}^{\infty} \frac{2}{\pi H_n^{(1)}(kR)} \int_0^\pi \varphi(\theta) \sin(n\theta) d\theta H_n^{(1)}(kr) \sin(n\theta),$$

where  $H_n^{(1)}$  is the first kind Hankel function of order  $n$ . Let  $\nu$  be the unit normal on  $\partial B_R^+$  directed into the infinite domain  $D$ . Then the normal derivative on  $\partial B_R^+$  can be written as

$$\frac{\partial u^s}{\partial r}(R, \theta) = \frac{2k}{\pi} \sum_{n=1}^{\infty} \frac{(H_n^{(1)})'(kR)}{H_n^{(1)}(kR)} \int_0^{\pi} \varphi(\theta) \sin(n\theta) d\theta \sin(n\theta).$$

Define the Dirichlet-to-Neumann map  $\mathcal{T}$  ( $\varphi \rightarrow \frac{\partial u^s}{\partial r}$ ) as

$$(\mathcal{T}\varphi)(\theta) = \frac{2k}{\pi} \sum_{n=1}^{\infty} \frac{(H_n^{(1)})'(kR)}{H_n^{(1)}(kR)} \int_0^{\pi} \varphi(\theta) \sin(n\theta) d\theta \sin(n\theta). \quad (4.4)$$

**Lemma 4.2.1.** *The Dirichlet-to-Neumann map  $\mathcal{T}$  is bounded from  $\tilde{\mathcal{H}}^{1/2}(\partial B_R^+)$  to its dual space  $(\tilde{\mathcal{H}}^{1/2}(\partial B_R^+))'$ .*

**Proof.** For any  $\varphi, \psi \in \tilde{\mathcal{H}}^{1/2}(\partial B_R^+)$ , let  $c_n = \frac{(H_n^{(1)})'(kR)}{H_n^{(1)}(kR)}$ . Then

$$\langle \mathcal{T}\varphi, \psi \rangle = \int_{\partial B_R^+} \mathcal{T}\varphi \bar{\psi} ds = kR \int_0^{\pi} \sum_{n=1}^{\infty} c_n \varphi_n \sin(n\theta) \bar{\psi} d\theta = \frac{k\pi R}{2} \sum_{n=1}^{\infty} c_n \varphi_n \bar{\psi}_n.$$

Here,

$$\varphi_n = \frac{2}{\pi} \int_0^{\pi} \varphi(\theta) \sin(n\theta) d\theta \quad \text{and} \quad \psi_n = \frac{2}{\pi} \int_0^{\pi} \psi(\theta) \sin(n\theta) d\theta.$$

From the recurrence relation of Hankel functions [2],

$$c_n = \frac{(H_n^{(1)})'(kR)}{H_n^{(1)}(kR)} = \frac{-H_{n+1}^{(1)}(kR) + \frac{n}{kR} H_n^{(1)}(kR)}{H_n^{(1)}(kR)} = \frac{-H_{n+1}^{(1)}(kR)}{H_n^{(1)}(kR)} + \frac{n}{kR},$$

Thus  $|c_n| \leq 1 + \frac{n}{kR} \leq c\sqrt{1+n^2}$  for some positive constant  $c$ .

Now

$$\begin{aligned} |\langle \mathcal{T}\varphi, \psi \rangle| &\leq \frac{ck\pi R}{2} \sum_{n=1}^{\infty} \sqrt{1+n^2} |\varphi_n \bar{\psi}_n| \\ &\leq \frac{ck\pi R}{2} \left( \sum_{n=1}^{\infty} \sqrt{1+n^2} |\varphi_n|^2 \right)^{1/2} \left( \sum_{n=1}^{\infty} \sqrt{1+n^2} |\psi_n|^2 \right)^{1/2}, \end{aligned}$$

i.e.,

$$|\langle \mathcal{T}\varphi, \psi \rangle| \leq \frac{ck\pi R}{2} \|\varphi\|_{\tilde{\mathcal{H}}^{1/2}} \|\psi\|_{\tilde{\mathcal{H}}^{1/2}}.$$

The proof is now complete.  $\square$

### 4.2.3 Well-posedness of the Forward Scattering Problem in Bounded Domain

The normal derivative of the total field is given by

$$\frac{\partial u}{\partial \nu} = \frac{\partial u^s}{\partial \nu} + \frac{\partial u^i}{\partial \nu} + \frac{\partial u^r}{\partial \nu} = \mathcal{T}(u) - \mathcal{T}(u^i + u^r) + \frac{\partial u^i}{\partial \nu} + \frac{\partial u^r}{\partial \nu}.$$

Denote  $g = \frac{\partial u^i}{\partial \nu} + \frac{\partial u^r}{\partial \nu} - \mathcal{T}(u^i + u^r)$ , then the total field satisfies the following boundary value problem:

$$\begin{cases} \Delta u + k^2 u = 0 & \text{in } D_R, \\ u = 0 & \text{on } \Gamma, \\ \frac{\partial u}{\partial \nu} = \mathcal{T}(u) + g & \text{on } \partial B_R^+. \end{cases} \quad (4.5)$$

Next, we address the well-posedness of the scattering problem (4.5), which also provides the basis for the analysis of the domain derivative of the forward scattering map in the next section.

Define a subspace of  $\mathcal{H}^1(D_R)$

$$\tilde{\mathcal{H}}_0^1(D_R) := \{ u \in \mathcal{H}^1(D_R) \mid u = 0 \text{ on } \Gamma, u|_{\partial B_R^+} \in \tilde{\mathcal{H}}^{1/2}(\partial B_R^+) \}.$$

By introducing the bilinear form

$$a(u, w) = \int_{D_R} \nabla u \cdot \nabla \bar{w} - k^2 u \bar{w} \, dx - \langle \mathcal{T}u, w \rangle$$

for  $u, w \in \tilde{\mathcal{H}}_0^1(D_R)$ , then  $u \in \tilde{\mathcal{H}}_0^1(D_R)$  is a weak solution of the boundary value problem (4.5) if

$$a(u, w) = \langle g, w \rangle \quad \text{for all } w \in \tilde{\mathcal{H}}_0^1(D_R). \quad (4.6)$$

**Theorem 4.2.2.** *The variational problem (4.6) attains a unique solution. Moreover,*

$$\|u\|_{1, D_R} \leq C \|g\|_{\left(\tilde{\mathcal{H}}^{1/2}(\partial B_R^+)\right)'}$$

for some positive constant  $C$ .

**Proof.** First we prove a Gårding type inequality. It is easy to show that

$$\langle \mathcal{T}u, u \rangle = \frac{k\pi R}{2} \sum_{n=1}^{\infty} c_n |u_n|^2, \quad (4.7)$$

where

$$c_n = \frac{(H_n^{(1)})'(kR)}{H_n^{(1)}(kR)}, \text{ and } u_n = \frac{2}{\pi} \int_0^\pi u(\theta) \sin(n\theta) d\theta.$$

Note that  $H_n^{(1)} = J_n + i Y_n$ , where  $J_n$  and  $Y_n$  are the first and second kind Bessel functions respectively, and the modulus of the Hankel function is a decreasing function [2], then

$$\Re c_n = \frac{J_n(kR)J_n'(kR) + Y_n(kR)Y_n'(kR)}{J_n^2(kR) + Y_n^2(kR)} = \frac{1}{2} \frac{(J_n^2)'(kR) + (Y_n^2)'(kR)}{J_n^2(kR) + Y_n^2(kR)} < 0. \quad (4.8)$$

Here  $\Re$  denotes the real part of a function.

From (4.7) and (4.8) it follows that  $\Re(\langle \mathcal{T}u, u \rangle) < 0$ . Consequently

$$\Re a(u, u) \geq \|u\|_{1, D_R}^2 - \tilde{c} \|u\|_{0, D_R}^2$$

for some positive constant  $\tilde{c}$ .

To prove the existence of a weak solution, from the Fredholm alternative we only need to prove the uniqueness. If  $a(u, w) = 0$  for any  $w \in \tilde{\mathcal{H}}_0^1(D_R)$ , then the imaginary part of  $a(u, u)$

$$\Im a(u, u) = -\Im \langle \mathcal{T}u, u \rangle = -\frac{k\pi R}{2} \sum_{n=1}^{\infty} \Im c_n |u_n|^2 = 0.$$

By the Wronskian formula [2],

$$\Im c_n = \frac{J_n(kR)Y_n'(kR) - Y_n(kR)J_n'(kR)}{J_n^2(kR) + Y_n^2(kR)} = \frac{2}{k\pi R} \frac{1}{J_n^2(kR) + Y_n^2(kR)} > 0.$$

Hence  $u_n = 0$  for all  $n$ . Note that  $u \in \tilde{\mathcal{H}}_0^1(D_R)$ , therefore  $u = 0$  on  $\partial B_R^+$ , and  $\mathcal{T}u = 0$  by definition. On the other hand,  $g = 0$  implies that  $\frac{\partial u}{\partial \nu} = \mathcal{T}u = 0$  on  $\partial B_R^+$ . Now  $u \equiv 0$  in  $D_R$  follows from the unique continuation result [41].

The continuous dependence of the solution on  $g$  follows from the Lax-Milgram lemma and the Fredholm alternative.  $\square$

### 4.3 Domain Derivative of the Forward Scattering Map

The theory of shape sensitivity analysis has been studied extensively for various shape optimization problems. We refer the reader to [52, 56] for detailed discussions and references. For the inverse scattering problem, Kirsch rigorously derived the domain derivative of the far-field operator for a  $C^2$  bounded obstacle in [44]. In this section, we derive the domain derivative of the operator that maps  $\Gamma$  to the measurement  $u|_{\partial B_R^+}$  (Theorem 4.3.1).

Define the forward mapping  $\mathcal{M} : \Gamma \rightarrow u|_{\partial B_R^+}$ . It maps the local surface displacement to the measurement on the half circle  $\partial B_R^+$ . The vector field  $V(x)$  is defined on  $\Gamma$ . It is assumed that  $V(x) \in C_0^2(\Gamma; \mathbb{R}^2)$ , i.e., twice continuously differentiable with compact support  $\text{supp}V \subset\subset \Gamma$ . For a given vector field  $V(x)$ , denote

$$\Gamma_\delta = \{x + \delta \cdot V(x) \mid x \in \Gamma, V(x) \in C_0^2(\Gamma; \mathbb{R}^2)\}$$

as the perturbation of  $\Gamma$  with  $V(x)$ . Now the domain derivative of the forward mapping  $\mathcal{M}$  with respect to the direction  $V(x)$  is defined as

$$\mathcal{M}'(\Gamma) := \lim_{\delta \rightarrow 0} \frac{M(\Gamma_\delta) - M(\Gamma)}{\delta}. \quad (4.9)$$

**Theorem 4.3.1.** *Let  $u$  be the solution to (4.1)-(4.3). If  $\Gamma$  is  $C^2$ ,  $V \in C_0^2(\Gamma; \mathbb{R}^2)$ , then the domain derivative  $\mathcal{M}'(\Gamma)$  exists. Moreover,  $\mathcal{M}'(\Gamma) = u'|_{\partial B_R^+}$ , where  $u'$  solves*

$$\begin{cases} \Delta u' + k^2 u' = 0 & \text{in } D_R, \\ u' = -(V \cdot \nu) \frac{\partial u}{\partial \nu} & \text{on } \Gamma, \\ \frac{\partial u'}{\partial \nu} = \mathcal{T}(u') & \text{on } \partial B_R^+. \end{cases} \quad (4.10)$$

Here  $\nu$  is the unit normal on  $\Gamma$  directed into the infinite domain  $D$ .

**Proof.** Let  $\delta$  be a small real number. The scattered field  $u^\delta$  produced by the scattering from the perturbed profile  $\Gamma_\delta$  satisfies the boundary value problem

$$\begin{cases} \Delta u^\delta + k^2 u^\delta = 0 & \text{in } D_R^\delta, \\ u^\delta = 0 & \text{on } \Gamma_\delta, \\ \frac{\partial u^\delta}{\partial \nu} = \mathcal{T}(u^\delta) + g & \text{on } \partial B_R^+, \end{cases}$$

where  $D_R^\delta$  is the domain bounded by  $\Gamma_\delta$  and  $\partial B_R^+$ . The weak solution of this bound-

ary value problem  $u^\delta \in \tilde{\mathcal{H}}_0^1(D_R^\delta)$  satisfies

$$a^\delta(u^\delta, w^\delta) = \langle g, w^\delta \rangle \quad \text{for all } w^\delta \in \tilde{\mathcal{H}}_0^1(D_R^\delta), \quad (4.11)$$

where

$$a^\delta(u^\delta, w^\delta) = \int_{D_R^\delta} \nabla u^\delta \cdot \nabla \overline{w^\delta} - k^2 u^\delta \overline{w^\delta} \, dx - \langle \mathcal{T} u^\delta, w^\delta \rangle. \quad (4.12)$$

We extend the definition of  $V \in C_0^2(\Gamma; \mathbb{R}^2)$  to the closure of the bounded domain  $D_R$ , which is denoted by  $\overline{D}_R$ , such that  $V(x)$  is  $C^2$  for  $x \in \overline{D}_R$  and  $V(x) = [0, 0]^T$  if  $|x| > R - \alpha$  for some small positive constant  $\alpha$ . Define the mapping  $\Psi(y)$  by letting

$$x = \Psi(y) = y + \delta V(y) \quad \text{for } y \in D_R.$$

Clearly,  $\Psi$  is a  $C^2$  mapping from  $D_R \rightarrow D_R^\delta$ . Denote the inverse map of  $\Psi(y)$  as  $\Phi(x)$ , which maps  $D_R^\delta \rightarrow D_R$ .

Let  $\tilde{u}^\delta(y) = u^\delta(\Psi(y))$ ,  $\tilde{w}^\delta(y) = w^\delta(\Psi(y))$ . It follows that  $\frac{\partial u^\delta}{\partial x_i} = \sum_{m=1}^2 \frac{\partial \tilde{u}^\delta}{\partial y_m} \frac{\partial \Phi_m}{\partial x_i}$ , where  $\Phi_m$  is the  $m$ th component of  $\Phi$ . Therefore, the bilinear form (4.12) can be written as

$$a^\delta(u^\delta, w^\delta) = \int_{D_R} \left[ \sum_{m,n=1}^2 b_{mn} \frac{\partial \tilde{u}^\delta}{\partial y_m} \frac{\partial \overline{\tilde{w}^\delta}}{\partial y_n} - k^2 \tilde{u}^\delta \overline{\tilde{w}^\delta} \right] J \, dy - \langle \mathcal{T} \tilde{u}^\delta, \tilde{w}^\delta \rangle.$$

Here,  $b_{mn} = \sum_{i=1}^2 \frac{\partial \Phi_m}{\partial x_i} \frac{\partial \overline{\Phi_n}}{\partial x_i}$ , the Jacobian  $J = \det D\Psi$ .

Define a new bilinear form  $\tilde{a}^\delta(\tilde{u}^\delta, w)$  by letting

$$\tilde{a}^\delta(\tilde{u}^\delta, w) = \int_{D_R} \left[ \sum_{m,n=1}^2 b_{mn} \frac{\partial \tilde{u}^\delta}{\partial y_m} \frac{\partial \overline{w}}{\partial y_n} - k^2 \tilde{u}^\delta \overline{w} \right] J \, dy - \langle \mathcal{T} \tilde{u}^\delta, w \rangle$$

for  $\tilde{u}^\delta, w \in \tilde{\mathcal{H}}_0^1(D_R)$ . Then the variational problem (4.11) is equivalent to finding  $\tilde{u}^\delta \in \tilde{\mathcal{H}}_0^1(D_R)$  such that

$$\tilde{a}^\delta(\tilde{u}^\delta, w) = \langle g, w \rangle \quad \text{for all } w \in \tilde{\mathcal{H}}_0^1(D_R). \quad (4.13)$$

From (4.6) and (4.13), it is easily seen that  $\tilde{u}^\delta - u$  satisfies

$$a(\tilde{u}^\delta - u, w) = -(\tilde{a}^\delta(\tilde{u}^\delta, w) - a(\tilde{u}^\delta, w)). \quad (4.14)$$

On the right hand side,

$$\begin{aligned} \tilde{a}^\delta(\tilde{u}^\delta, w) - a(\tilde{u}^\delta, w) &= \int_{D_R} \left[ \sum_{m,n=1}^2 b_{mn} \frac{\partial \tilde{u}^\delta}{\partial y_m} \frac{\partial \bar{w}}{\partial y_n} - k^2 \tilde{u}^\delta \bar{w} \right] J \, dy \\ &\quad - \int_{D_R} \nabla \tilde{u}^\delta \cdot \nabla \bar{w} - k^2 \tilde{u}^\delta \bar{w} \, dy. \end{aligned} \quad (4.15)$$

The coefficient matrix  $(b_{mn})$  and the Jacobian  $J$  can be further written as

$$\begin{aligned} J &= 1 + \delta \nabla \cdot V + O(\delta^2), \\ (b_{m,n})J &= I - \delta(\tilde{b}_{mn}) + O(\delta^2), \end{aligned} \quad (4.16)$$

where  $I$  is the  $2 \times 2$  identity matrix and the matrix

$$(\tilde{b}_{mn}) = \nabla V + (\nabla V)^T - (\nabla \cdot V)I. \quad (4.17)$$

Therefore, from (4.14) - (4.17) and the continuous dependence of  $\tilde{u}^\delta - u$  on the right hand side, it follows that

$$\left\| \tilde{u}^\delta - u \right\|_{1, D_R} \rightarrow 0 \quad \text{as } \delta \rightarrow 0.$$

Now

$$\begin{aligned}
a\left(\frac{\tilde{u}^\delta - u}{\delta}, w\right) &= -\frac{1}{\delta}(a^\delta(\tilde{u}^\delta, w) - a(\tilde{u}^\delta, w)) \\
&= \int_{D_R} \sum_{m,n=1}^2 \tilde{b}_{mn} \frac{\partial \tilde{u}^\delta}{\partial y_m} \frac{\partial \bar{w}}{\partial y_n} + k^2(\nabla \cdot V) \tilde{u}^\delta \bar{w} \, dy + O(\delta).
\end{aligned}$$

Since  $\left\| \tilde{u}^\delta - u \right\|_{1, D_R} \rightarrow 0$  as  $\delta \rightarrow 0$ ,

$$a\left(\frac{\tilde{u}^\delta - u}{\delta}, w\right) \rightarrow \int_{D_R} \sum_{m,n=1}^2 \tilde{b}_{mn} \frac{\partial u}{\partial y_m} \frac{\partial \bar{w}}{\partial y_n} + k^2(\nabla \cdot V) u \bar{w} \, dy \quad \text{as } \delta \rightarrow 0.$$

Hence the limit  $\lim_{\delta \rightarrow 0} \frac{\tilde{u}^\delta - u}{\delta}$  exists, which we denote as  $u_0$ .

Clearly,  $u_0$  is the solution to the following variational problem:

$$a(u_0, w) = \int_{D_R} \sum_{m,n=1}^2 \tilde{b}_{mn} \frac{\partial u}{\partial y_m} \frac{\partial \bar{w}}{\partial y_n} + k^2(\nabla \cdot V) u \bar{w} \, dy \quad (4.18)$$

for any  $w \in \tilde{\mathcal{H}}_0^1(D_R)$ . By the assumption that  $\Gamma$  is  $C^2$ , the scattered field  $u \in C^2(D) \cap C(\bar{D})$  [61]. Apply the formula (4.17), then for any  $w \in \tilde{\mathcal{H}}_0^1(D_R) \cap \mathcal{H}^2(D_R)$ ,

$$\begin{aligned}
&\sum_{m,n=1}^2 \tilde{b}_{mn} \frac{\partial u}{\partial y_m} \frac{\partial \bar{w}}{\partial y_n} \\
&= \nabla u^T (\nabla V + (\nabla V)^T - (\nabla \cdot V) I) \nabla \bar{w} \\
&= [\nabla(V \cdot \nabla \bar{w}) \cdot \nabla u - (\nabla(\nabla \bar{w}) V) \cdot \nabla u] + [\nabla(V \cdot \nabla u) \cdot \nabla \bar{w} \\
&\quad - (\nabla(\nabla u) V) \cdot \nabla \bar{w}] - \nabla u^T (\nabla \cdot V) I \nabla \bar{w} \\
&= \nabla(V \cdot \nabla \bar{w}) \cdot \nabla u + \nabla(V \cdot \nabla u) \cdot \nabla \bar{w} - \nabla \cdot [(\nabla u \cdot \nabla \bar{w}) V].
\end{aligned}$$

By the Green's formula and noting that  $V = 0$  on  $\partial B_R^+$ , (4.18) can be reduced to

$$\begin{aligned} a(u_0, w) &= \int_{D_R} -(V \cdot \nabla \bar{w}) \Delta u + \nabla(V \cdot \nabla u) \cdot \nabla \bar{w} + k^2(\nabla \cdot V) u \bar{w} \, dy \\ &\quad - \int_{\Gamma} (V \cdot \nabla \bar{w}) \frac{\partial u}{\partial \nu} - (\nabla u \cdot \nabla \bar{w})(V \cdot \nu) \, ds. \end{aligned}$$

On the other hand,  $u = w = 0$  on  $\Gamma$ , we have  $(V \cdot \nabla \bar{w}) \frac{\partial u}{\partial \nu} - (\nabla u \cdot \nabla \bar{w})(V \cdot \nu) = 0$  on  $\Gamma$ . Therefore,

$$\begin{aligned} a(u_0, w) &= \int_{D_R} k^2 u (V \cdot \nabla \bar{w}) + \nabla(V \cdot \nabla u) \cdot \nabla \bar{w} + k^2(\nabla \cdot V) u \bar{w} \, dy \\ &= \int_{D_R} \nabla(V \cdot \nabla u) \cdot \nabla \bar{w} - k^2(V \cdot \nabla u) \bar{w} \, dy + \int_{D_R} k^2 \nabla \cdot (u \bar{w} V) \, dy, \end{aligned}$$

where  $\int_{D_R} k^2 \nabla \cdot (u \bar{w} V) \, dy = 0$  by the Divergence theorem. We finally obtain

$$a(u_0, w) = \int_{D_R} \nabla(V \cdot \nabla u) \cdot \nabla \bar{w} - k^2(V \cdot \nabla u) \bar{w} \, dy \quad \text{for any } w \in \tilde{\mathcal{H}}_0^1(D_R) \cap \mathcal{H}^2(D_R). \quad (4.19)$$

It is easy to check that  $u_0$  defined above is the weak solution of the following boundary value problem

$$\begin{cases} \Delta u_0 + k^2 u_0 = (\Delta + k^2)(V \cdot \nabla u) & \text{in } D_R, \\ u_0 = 0 & \text{on } \Gamma, \\ \frac{\partial u_0}{\partial \nu} = \mathcal{T}(u_0) & \text{on } \partial B_R^+, \end{cases}$$

Let  $u' = u_0 - V \cdot \nabla u$ , then  $u'$  solves (4.10). Further, note that  $V = 0$  on  $\partial B_R^+$ , therefore

$$u' = u_0 = \lim_{\delta \rightarrow 0} \frac{\tilde{u}^\delta - u}{\delta} = \mathcal{M}'(\Gamma) \quad \text{on } \partial B_R^+.$$

The proof is now complete. □

## 4.4 Imaging with Multiple Frequency Data

### 4.4.1 Descent Direction for the Cost Functional

For a fixed wavenumber  $k$ , denote  $u^m$  as the measurement collected on  $\partial B_R^+$ . For a given curve  $\Gamma$ , define the cost functional

$$F(\Gamma) := \frac{1}{2} \|\mathcal{M}(\Gamma) - u^m\|_{L^2(\partial B_R^+)}^2.$$

A descent direction on  $\Gamma$  is a vector field  $V$  such that the cost functional decreases, i.e.,  $F(\Gamma_\delta) < F(\Gamma)$  if  $\delta \in (0, t_0]$  for some small positive constant  $t_0$ . We also call this descent direction  $V$  descent velocity. The perturbation of  $\Gamma$  may be viewed as an evolution process of assigning each point  $x$  on  $\Gamma$  a descent velocity  $V(x)$  and moving  $\Gamma$  with the velocity  $V(x)$  in a small artificial time interval  $[0, t_0]$ . The characterization of a descent velocity for the cost functional  $F(\Gamma_t)$  is established in the next theorem.

**Theorem 4.4.1.** *Let  $\Gamma$  be  $C^2$ ,  $\nu$  be the unit normal on  $\Gamma$  directed into the infinite domain  $D$ .  $u$  is the solution to the forward scattering problem (4.1)-(4.3), and  $u^*$  is the solution of the following boundary value problem:*

$$\begin{cases} \Delta u^* + k^2 u^* = 0 & \text{in } D_R, \\ u^* = 0 & \text{on } \Gamma, \\ \frac{\partial u^*}{\partial \nu} = \mathcal{T}^*(u^*) + u - u^m & \text{on } \partial B_R^+. \end{cases} \quad (4.20)$$

where  $\mathcal{T}^*$  is the adjoint operator of  $\mathcal{T}$ . If  $V \in C_0^2(\Gamma; \mathbb{R}^2)$ , and satisfies

$$- \int_{\Gamma} (V \cdot \nu) \cdot \Re \left[ \frac{\partial u}{\partial \nu} \frac{\partial \bar{u}^*}{\partial \nu} \right] ds < 0, \quad (4.21)$$

then  $\left. \frac{dF(\Gamma_t)}{dt} \right|_{t=0} < 0$ . Here  $\Re$  denotes the real part of a function.

**Proof.** Clearly,  $u$  also solves the boundary value problem (4.5). Let  $u'$  and  $u^*$  be the solution of (4.10) and (4.20), respectively. By the Green's formula,

$$\int_{\partial B_R^+} \frac{\partial u^*}{\partial \nu} \overline{u'} - u^* \overline{\frac{\partial u'}{\partial \nu}} ds = \int_{\Gamma} \frac{\partial u^*}{\partial \nu} \overline{u'} - u^* \overline{\frac{\partial u'}{\partial \nu}} ds. \quad (4.22)$$

Using the boundary conditions in (4.10) and (4.20), the identity (4.22) is reduced to

$$\int_{\partial B_R^+} \mathcal{T}^*(u^*) \overline{u'} ds + \int_{\partial B_R^+} (u - u^m) \overline{u'} ds - \int_{\partial B_R^+} u^* \overline{\mathcal{T}(u')} ds = - \int_{\Gamma} (V \cdot \nu) \frac{\partial u^*}{\partial \nu} \overline{\frac{\partial u}{\partial \nu}} ds.$$

Since  $\mathcal{T}^*$  is the adjoint operator of  $\mathcal{T}$ , we have

$$\int_{\partial B_R^+} (u - u^m) \overline{u'} ds = - \int_{\Gamma} (V \cdot \nu) \frac{\partial u^*}{\partial \nu} \overline{\frac{\partial u}{\partial \nu}} ds.$$

Therefore by Theorem 4.3.1,

$$\left. \frac{dF(\Gamma_t)}{dt} \right|_{t=0} = \Re \left\{ \int_{\partial B_R^+} (u - u^m) \overline{u'} ds \right\} = - \int_{\Gamma} (V \cdot \nu) \cdot \Re \left[ \frac{\partial u}{\partial \nu} \overline{\frac{\partial u^*}{\partial \nu}} \right] ds.$$

The assertion of the theorem holds.  $\square$

From (4.21), it is easily seen that in practice there are many possible choices for the descent direction  $V$  defined on  $\Gamma$ . In our case, since the local surface displacement is represented by the function  $f$ , we let  $V = [0, v]^T$ , where  $v \in C_0^2(\Gamma)$  is a compactly supported function on  $\Gamma$  satisfying the inequality

$$- \int_{\Gamma} (v \cdot \nu_2) \cdot \Re \left[ \frac{\partial u}{\partial \nu} \overline{\frac{\partial u^*}{\partial \nu}} \right] ds < 0. \quad (4.23)$$

Here  $\nu_2$  is the second component of the unit normal  $\nu$ . In particular, if  $v \cdot \nu_2 = \Re \left[ \frac{\partial u}{\partial \nu} \overline{\frac{\partial u^*}{\partial \nu}} \right]$ , then  $V$  is the steepest descent direction for the cost functional  $F(\Gamma_t)$ .

However,  $\Re \left[ \frac{\partial u}{\partial \nu} \frac{\partial \overline{u^*}}{\partial \nu} \right]$  may not be a smooth and compactly supported function on  $\Gamma$ . Therefore, we need to modify its definition to make it smooth and compactly supported. This can be accomplished by the cubic spline interpolation [28]. We denote the new smooth, compactly supported function as  $v_s$ . The choice of the smooth version  $v_s$  of  $v$  is a regularization procedure in the regularization theory for ill-posed problems.

#### 4.4.2 Reconstruction Scheme

Suppose that multiple frequency measurements  $\{ u_{k_j}^m \mid j = 1, 2, \dots, M \}$  on the half circle  $\partial B_R^+$  are available for a set of wavenumbers  $\{ k_j \mid j = 1, 2, \dots, M \}$ , where  $k_j > k_i$  if  $j > i$ . Starting from the flat surface as our initial guess, the proposed reconstruction method marches from  $k_1$  to  $k_M$ . At the fixed wavenumber  $k = k_j$ , by the cubic spline interpolation, a smooth version of the descent vector field  $V$  is defined, where  $V = [0, v]^T$  and  $v$  satisfies (4.23). The reconstructed profile evolves with the chosen descent velocity at the fixed wavenumber. This evolution process continues until  $k = k_M$ .

Let  $\Gamma^{rec}$  be the reconstruction,  $D^{rec}$  is the domain above the curve  $\Gamma^{rec} \cup \Gamma_0$ .  $D_R^{rec} := D^{rec} \cap B_R$  is the domain bounded by  $\Gamma^{rec}$  and  $\partial B_R^+$ . The reconstruction method with multiple frequency data is proposed as follows:

(1) (*Initialization*)

Let  $k = k_1$ , initially set  $\Gamma^{rec} = \{ (x_1, x_2) \mid x_1 \in (-R, R), x_2 = 0 \}$  (flat surface).

(2) (*Update the reconstruction by marching along the wavenumbers*)

**FOR**  $j = 1, 2, 3, \dots, M$

Let  $k = k_j$ ,

**FOR**  $n = 1, 2, 3, \dots, N$  (Evolution process at fixed wavenumber  $k$ ):

Choose the descent direction  $V_n = [0, v_n]$  s.t.  $v_n \in C_0^2(\Gamma)$  and

$$- \int_{\Gamma} (v_n \cdot \nu_2) \cdot \Re \left[ \frac{\partial u}{\partial \nu} \frac{\partial \bar{u}^*}{\partial \nu} \right] ds < 0, \quad \text{where}$$

$$\begin{cases} \Delta u + k^2 u = 0 & \text{in } D_R^{rec}, \\ u = 0 & \text{on } \Gamma^{rec}, \\ \frac{\partial u}{\partial \nu} = \mathcal{T}(u) + g & \text{on } \partial B_R^+. \end{cases} \quad \begin{cases} \Delta u^* + k^2 u^* = 0 & \text{in } D_R^{rec}, \\ u^* = 0 & \text{on } \Gamma^{rec}, \\ \frac{\partial u^*}{\partial \nu} = \mathcal{T}^*(u^*) + u - u_k^m & \text{on } \partial B_R^+. \end{cases}$$

Update:  $\Gamma^{rec} \leftarrow \Gamma^{rec} + \alpha_n V_n$ ,  $\alpha_n$  is the step length.

**END**

**END**

**Remark 5.1** *The lowest wavenumber  $k_1$  has to be small to guarantee that the main features of the profile are captured. Based on the numerical investigation, one basic rule to follow is  $1/k_1 \geq R$ , i.e., the wavelength  $\lambda_1$  corresponding to the lowest wavenumber  $k_1$  is at least comparable to  $R$ . The restriction may be due to the reason that the reconstruction with the measurement  $u_{k_1}^m$  usually captures the feature of order  $\lambda_1$ , which needs to be sufficiently large in order that the main feature of the profile (of order  $R$ ) is recovered in our approach. Without loss of generality, it is assumed that  $R = 1$  and  $k_1 = 1$ . On the other hand,  $1/k_M$  has to be smaller than the scale of the fine features of the profile such that the small details of the target are accurately reconstructed as well.*

**Remark 5.2** *Theorem 4.4.1 does not require that  $\Gamma$  be parameterized by some function  $f$ . In fact the assertion of the theorem is valid for any  $C^2$  local disturbance  $\Gamma$ . Therefore, our proposed method can be modified to deal with more general cases. The corresponding descent direction may be chosen to be parallel to  $\nu$  such that  $V = v \cdot \nu$*

and  $v = \Re \left[ \frac{\partial u}{\partial \nu} \frac{\partial \bar{u}^*}{\partial \nu} \right]$ . The evolution process of  $\Gamma$  with the descent velocity  $V$  can be simulated by the level set method.

At low wavenumbers, the reconstruction captures the main features of the local disturbance (low frequency modes). It also serves as the starting point for the reconstruction at the next higher wavenumber, where the evolution process continues to recover the fine features of the local disturbance (high frequency modes). Ideally, the smaller the increment  $k_{j+1} - k_j$  is, the better reconstruction image would be. In fact, the increment parameter  $k_{j+1} - k_j$  depends on the scale feature of the real profile. If  $k_{j+1} - k_j$  is too large, the reconstruction procedure may fail to recover the Fourier modes of the real profile between  $k_j$  and  $k_{j+1}$ . From numerical simulations discussed in the next section,  $k_{j+1} - k_j = 2$  is sufficient to obtain accurate reconstruction.

It is also worth pointing out that the reconstruction with only the single highest wavenumber  $k = k_M$  will not yield a satisfactory image, as the convergence to the global minimizer of the cost functional strongly relies on the initial guess. In practice, a good initial guess is hard to choose without *a priori* information of the imaging target. This may be confirmed by numerical simulations presented in the next section. However, the reconstruction with multiple frequency data overcomes the difficulty of reaching some local minimum. Starting from the flat surface as an initial guess, the reconstructed image captures the large scale features of the profile at a lower wavenumber  $k_j$ , which serves as the initial guess for the reconstruction at a higher wavenumber  $k_{j+1}$ .

## 4.5 Numerical Examples

### 4.5.1 Numerical approximation of the forward scattering problem

We need to calculate only  $\frac{\partial u}{\partial \nu}$  and  $\frac{\partial u^*}{\partial \nu}$  on  $\Gamma_{rec}$  to define a descent direction at a fixed wavenumber, the solution  $u$  and  $u^*$  in the interior domain need not be calculated. Hence the boundary integral equation method may be applied to solve the forward problem, which is fast and reduces the complexity of the computation by solving a much smaller linear system compared to the finite element method. In particular, the boundary integral equation method can handle the high wavenumber problem.

Let  $\Phi(x, y) = \frac{i}{4}H_0^{(1)}(k|x-y|)$  be the fundamental solution for the Helmholtz equation in  $\mathbb{R}^2$ . The solution  $u$  to (4.5) satisfies the following system of integral equations:

$$\begin{aligned} \frac{1}{2}u(x) + \int_{\Gamma_{rec}} \frac{\partial u(y)}{\partial \nu y} \Phi(x, y) ds_y - \int_{\partial B_R^+} (\mathcal{T}u)(y) \Phi(x, y) ds_y \\ + \int_{\partial B_R^+} \frac{\partial \Phi(x, y)}{\partial \nu y} u(y) ds_y = \int_{\partial B_R^+} g(y) \Phi(x, y) ds_y \quad x \in \partial B_R^+, \end{aligned}$$

$$\begin{aligned} \int_{\Gamma_{rec}} \frac{\partial u(y)}{\partial \nu y} \Phi(x, y) ds_y - \int_{\partial B_R^+} (\mathcal{T}u)(y) \Phi(x, y) ds_y + \int_{\partial B_R^+} \frac{\partial \Phi(x, y)}{\partial \nu y} u(y) ds_y \\ = \int_{\partial B_R^+} g(y) \Phi(x, y) ds_y \quad x \in \Gamma_{rec}. \end{aligned}$$

Similarly, we calculate  $\frac{\partial u^*}{\partial \nu}$  on  $\partial B_R^+$  by solving the system

$$\begin{aligned} \frac{1}{2}u^*(x) + \int_{\Gamma_{rec}} \frac{\partial u^*(y)}{\partial \nu_y} \Phi(x, y) ds_y - \int_{\partial B_R^+} (\mathcal{T}^* u^*)(y) \Phi(x, y) ds_y \\ + \int_{\partial B_R^+} \frac{\partial \Phi(x, y)}{\partial \nu_y} u^*(y) ds_y = \int_{\partial B_R^+} (u(y) - u^m(y)) \Phi(x, y) ds_y \quad x \in \partial B_R^+, \end{aligned}$$

$$\begin{aligned} \int_{\Gamma_{rec}} \frac{\partial u^*(y)}{\partial \nu_y} \Phi(x, y) ds_y - \int_{\partial B_R^+} (\mathcal{T}^* u^*)(y) \Phi(x, y) ds_y + \int_{\partial B_R^+} \frac{\partial \Phi(x, y)}{\partial \nu_y} u^*(y) ds_y \\ = \int_{\partial B_R^+} (u(y) - u^m(y)) \Phi(x, y) ds_y \quad x \in \Gamma_{rec}. \end{aligned}$$

## 4.5.2 Imaging of the local surface displacement

Several numerical examples are presented to illustrate the efficiency of the proposed method. Example 1 considers a smooth upward profile ( $f \geq 0$ ), the convergence of the reconstruction is highlighted. We also compare the reconstruction with the image when only the single highest wavenumber is used. In Example 2, we remove the restriction that  $f \geq 0$ . The surface displacement is represented by a general smooth function  $f$ , where  $\Gamma_+ := \{ (x_1, f) \mid x_1 \in (-R, R), f(x_1) > 0 \}$  and  $\Gamma_- := \{ (x_1, f) \mid x_1 \in (-R, R), f(x_1) < 0 \}$  are both nonempty sets. Example 3 discusses the reconstruction for the piecewise linear (nonsmooth) local surface displacement. In the last example, the reconstruction of a multiscale profile is presented. In all simulations, we use noisy data by adding 5% additive noise to the measurements.

### Example 1. Smooth upward profile

$$f(x_1) = \begin{cases} 0.2 + 0.2 \cos(4\pi x_1 + \pi) & x_1 \in [-0.5, 0), \\ 0.1 + 0.1 \cos(4\pi x_1 + \pi) & x_1 \in [0, 0.5], \\ 0 & \text{elsewhere.} \end{cases}$$

The boundary of the whole obstacle is  $C^1$  (Figure 4.2 left). An incident wave  $u^i = e^{ikd \cdot x}$  with normal incident direction impinges on the obstacle. The wavenumbers  $k_1 = 1$  and  $k_M = 20$ . The reconstruction  $f_n$  when  $k = 16$  and the real profile  $f$  are plotted in Figure 4.2 (right). It is observed that the reconstruction is accurate even though noise is present in measurements. To test the convergence of the proposed method, the relative error with respect to the wavenumber is shown in Figure 4.3. Here the relative error is defined as

$$\frac{\left( \int_{-R}^R |f(x_1) - f_n(x_1)|^2 dx_1 \right)^{1/2}}{\left( \int_{-R}^R |f(x_1)|^2 dx_1 \right)^{1/2}}.$$

It is clear that the relative error decreases until the main Fourier modes of  $f$  are recovered. Figure 4.4 illustrates the reconstructions for various wavenumbers. At low wavenumbers, the reconstruction captures the main features of the real profile, while the fine features of the profile is recovered as the evolution process continues.

Next is the case when only the single highest frequency measurement is used.

Figure 4.5 (left) presents the relative residual  $\frac{\left\| \mathcal{M}(\Gamma_{rec}) - u_{k_M}^m \right\|_{L^2(\partial B_R^+)}}{\left\| u_{k_M}^m \right\|_{L^2(\partial B_R^+)}}$  for the evolution process at  $k = k_M$  when only the single frequency is applied. It is clear that the reconstruction reaches some local minimum of the cost functional. The residual decreases and stagnates around 0.2 after 40 iterations. The corresponding image is shown in Figure 5 (right, dash line), which deviates greatly from the real profile. As pointed out previously, in this case the convergence to the global minimizer of the

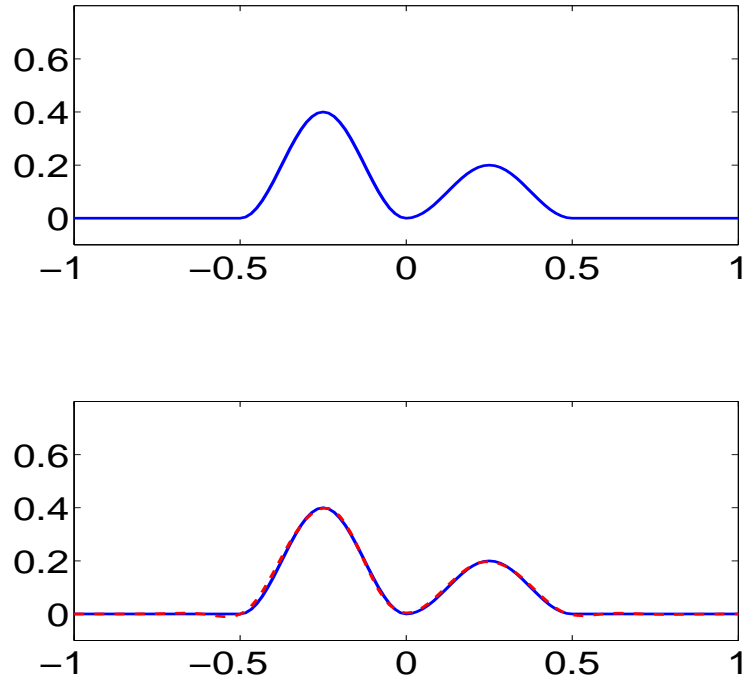


Figure 4.2: Top: real profile. Bottom: reconstruction (dash line) at  $k = 16$  compared with the real curve (solid line).

cost functional strongly relies on the initial guess, which is hard to choose without *a priori* information of the imaging target. Multiple frequency data overcomes the difficulty, since the reconstruction at each lower frequency serves as the initial guess for the reconstruction at the higher frequency.

### Example 2. General smooth profile

In this example, the surface displacement is represented by a general smooth function  $f = f_1 + f_2$  (solid line in Figure 4.6), where

$$f_1(x_1) = \begin{cases} 0.2(\cos(\frac{5\pi}{2}x_1) - 1) + 0.05(1 + \cos(\frac{5\pi}{2}x_1 + \pi)) & x_1 \in [-\frac{4}{5}, 0), \\ 0.2(\cos(\frac{5\pi}{2}x_1) - 1) & x_1 \in [0, \frac{4}{5}], \\ 0 & \text{elsewhere} \end{cases}$$

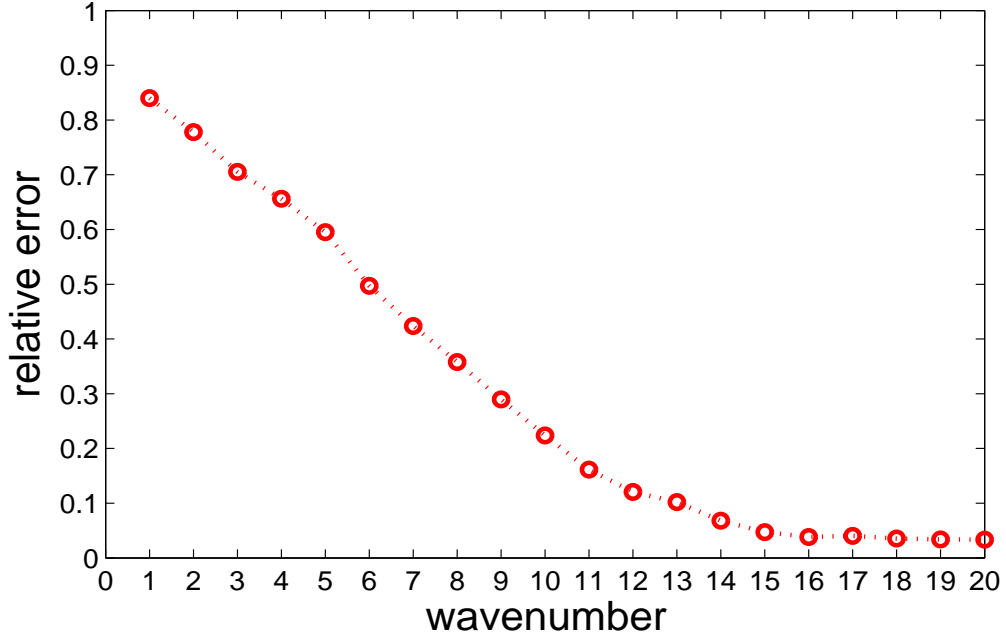


Figure 4.3: Relative error with respect to the wavenumber.

and

$$f_2(x_1) = \begin{cases} \exp\left(\frac{1}{\left(\frac{5}{4}x_1\right)^2 - 1}\right) & |x_1| < \frac{4}{5}, \\ 0 & \text{elsewhere.} \end{cases}$$

Here  $\Gamma_+ := \{ (x_1, f) \mid x_1 \in (-R, R), f(x_1) > 0 \}$  and  $\Gamma_- := \{ (x_1, f) \mid x_1 \in (-R, R), f(x_1) < 0 \}$  are both nonempty sets. We set  $k_M = 30$ , and the final reconstruction with 5% noise in measurements is plotted in Figure 4.6 (dash line).

Figure 4.7 shows the relative error for various wavenumbers.

The proposed reconstruction method with multiple frequency data again gives a stable and accurate reconstruction of the general profile. However, compared with the profile considered in Example 1, the convergence rate decreases when the non-negativity or non-positivity assumption is removed from the imaging target. (see Figure 4.3 and Figure 4.7).

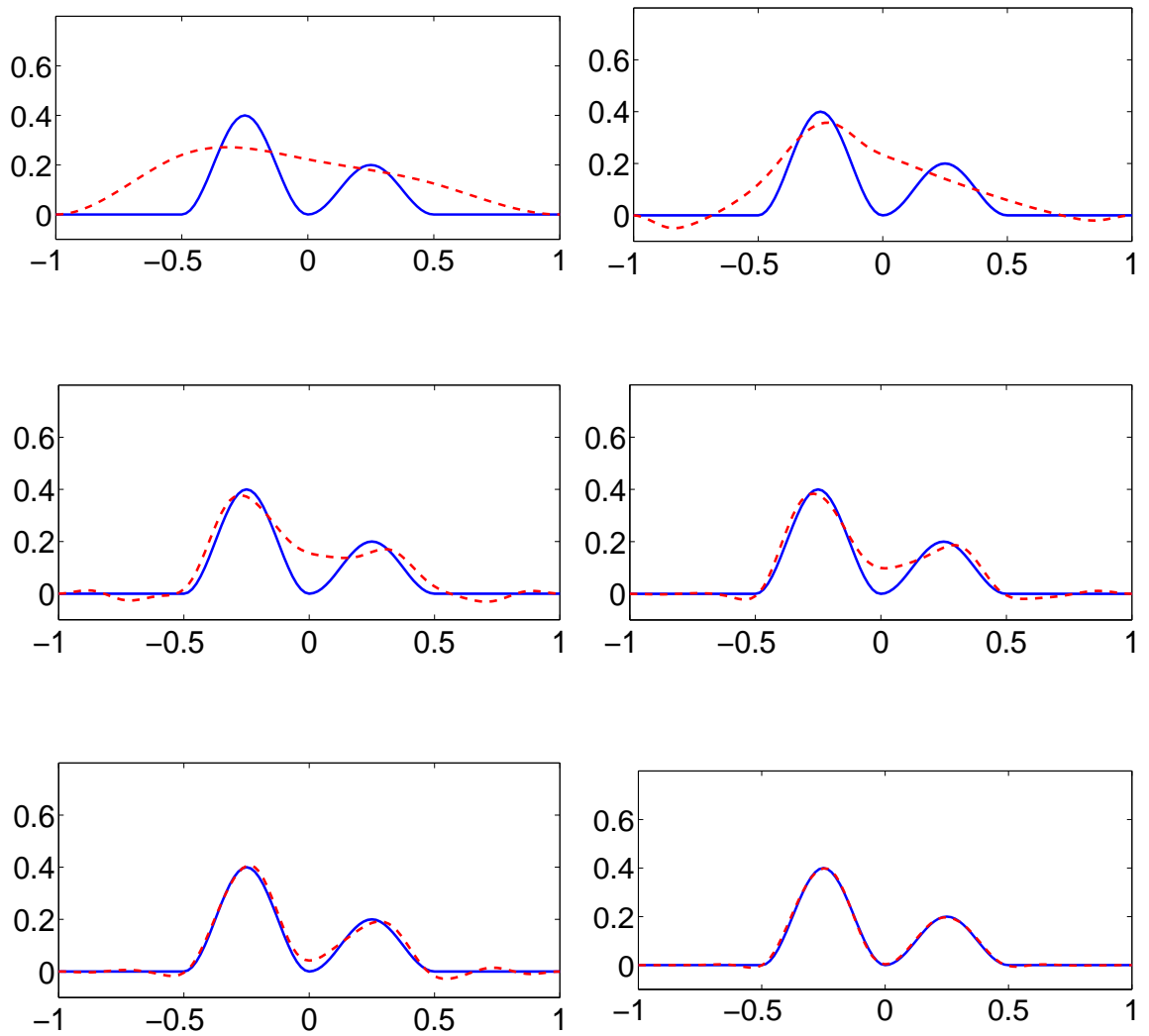


Figure 4.4: Evolution of the reconstruction at  $k = 1, 5, 8, 10, 12, 16$  (dash line, left to right, top to bottom).

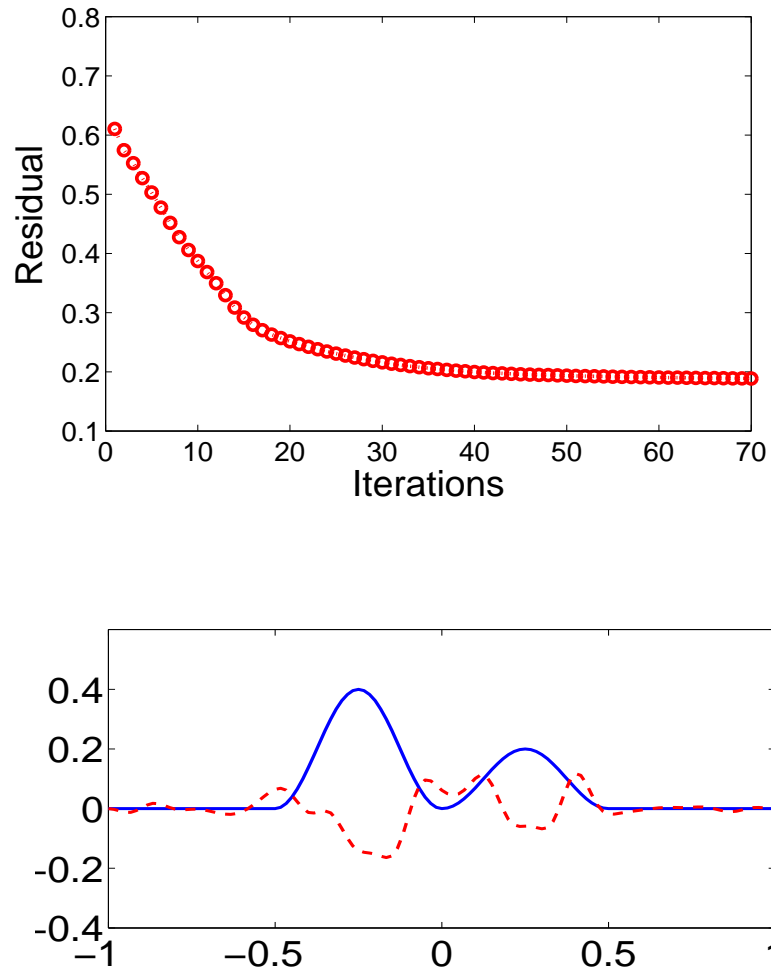


Figure 4.5: Top: relative residual with respect to the iteration number at  $k = k_M$  when only single frequency data is used. Bottom: reconstruction (dash line) with single frequency only.

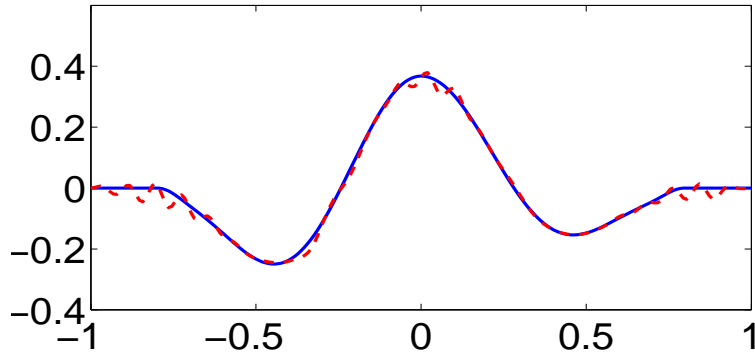


Figure 4.6: Reconstruction (dash line) at  $k = 30$  compared with the real curve (solid line).

### Example 3. Piecewise linear profile

The previous examples assume some regularity on the local surface displacement. Next we consider a piecewise linear profile (the solid line in Figure 4.8). By using our method, the reconstruction  $f_n$  captures the position and height of bumps (where  $f > 0$ ) accurately when  $k_M = 16$  (the dash line in Figure 4.8). The corner of the profile is also approximated with reasonable accuracy by the  $C^2$  smooth reconstructed function. It will be interesting to develop a regularization strategy to approximate the corner with some non-smooth function, which will be investigated in our future work.

### Example 4. Multiscale profile

The multiscale profile is represented by

$$f(x_1) = \begin{cases} 0.13 + 0.1 \cos\left(\frac{8\pi}{5}x_1 + \pi\right) + 0.03 \cos(16\pi x_1 + \pi) & x_1 \in \left[-\frac{3}{4}, \frac{1}{2}\right], \\ 0 & \text{elsewhere.} \end{cases}$$

It consists of two scales. The macroscale feature of the profile is represented by the

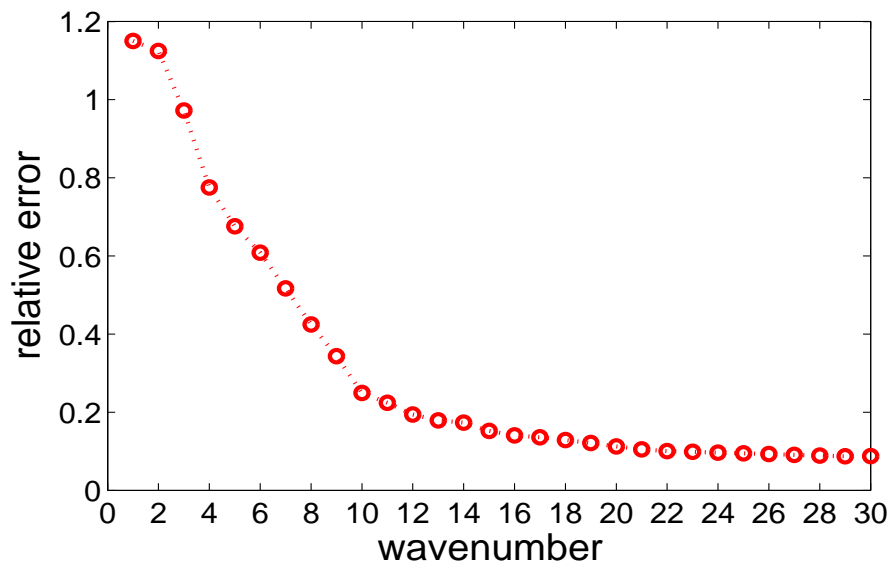


Figure 4.7: Relative error with respect to the wavenumber.

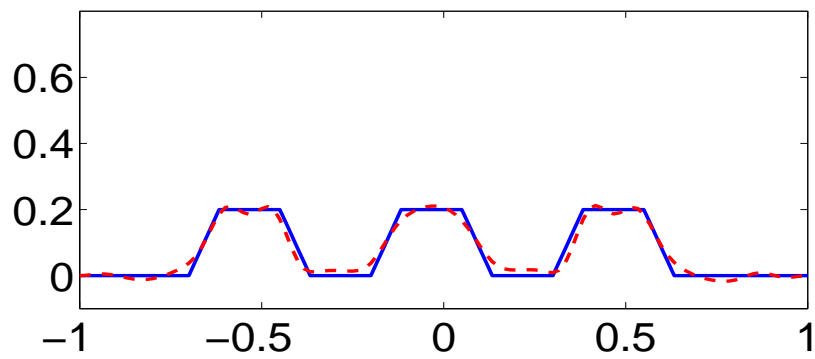


Figure 4.8: Reconstruction (dash line) at  $k = 16$  compared with the real curve (solid line).

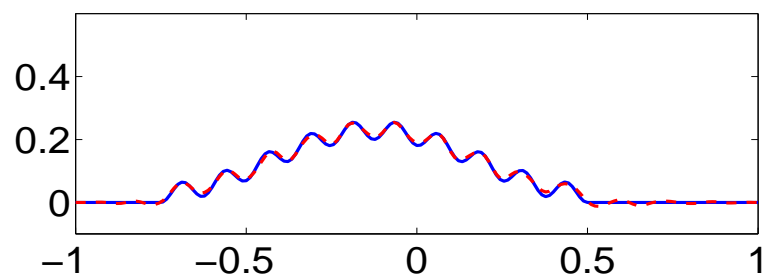
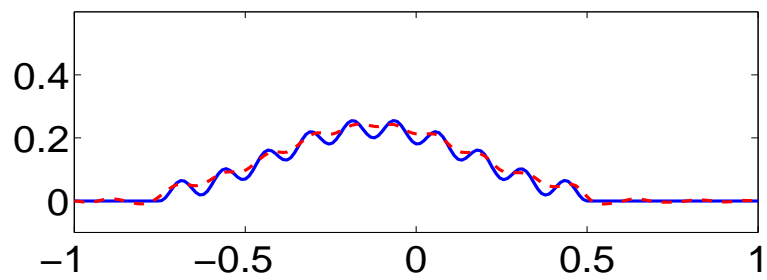
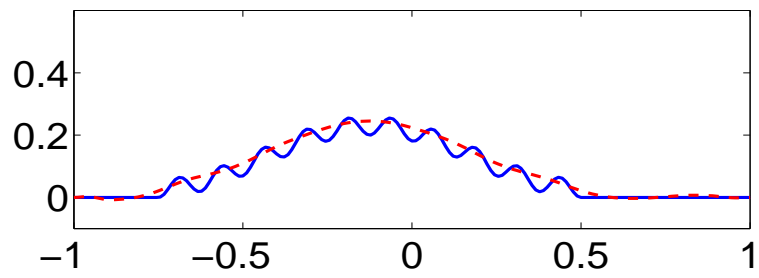
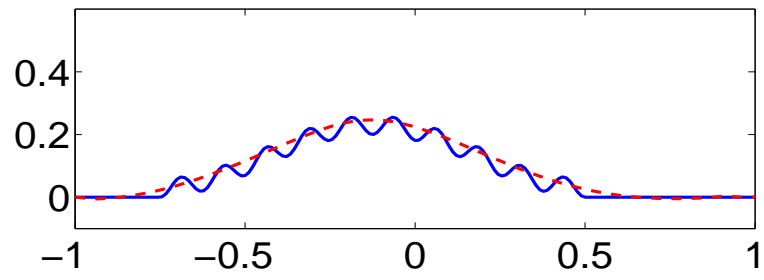


Figure 4.9: Reconstruction at  $k = 10, 20, 33, 40$  (dash line, top to bottom) compared with the real curve (solid line).

function  $0.13 + 0.1 \cos(\frac{8\pi}{5}x_1 + \pi)$  ; while the microscale is represented by function  $0.03 \cos(16\pi x_1 + \pi)$  with period  $\frac{1}{8}$ . The reconstruction captures the macroscale features when  $k = 10$  (Figure 4.9, top left). To recover the fine details of the profile with the period  $\frac{1}{8}$ ,  $k$  needs to be sufficiently high. Here, microscale features are captured when  $k = 40$  (Figure 4.9, bottom right). The whole local disturbance is accurately reconstructed with noisy data. On the other hand, it is observed that the resolution of the reconstruction does not improve much from  $k = 10$  to  $k = 33$ . This is due to the fact that other than the macroscale feature, no scale length of the profile is comparable with the corresponding wavelength for  $k \in (10, 33)$ .

# Chapter 5

## Conclusion

This thesis is the initial endeavor in the whole picture of the near-field imaging. We focus on one specific problem, where the local surface displacement on an infinite ground plane is the imaging target. The main contribution is the explicit formulation of the connection between the evanescent wave modes and the high frequency components of the surface displacement, and a new numerical scheme to reconstruct the surface displacement that extracts the information carried by the evanescent modes effectively. Numerical examples show that images with a resolution of  $\lambda/10$  are obtained. For the general local surface displacement, a reconstruction scheme with multiple frequency data is proposed that captures the main (large scale) features at low frequencies and recovers the fine details at high frequencies.

Numerical evidences confirm that the resolution in the near-field regime can be significantly improved. However, theoretical study on the uniqueness and the stability estimates remain open. In particular, the stability estimate which is able to incorporate explicitly the dependence on the distance  $d$  would help to understand the ill-posedness of the inverse scattering problem better in the near field.

There are also many related imaging problems that arise in biological and nanosciences. For example, the imaging of the human cancer cell in the near-field regime,

which turns out to be an inverse medium scattering problem. Though the evanescent wave modes carried by the scattered field is available in the near-field measurement, the relation between such evanescent wave modes and the high frequency components of the medium is completely open. Such relation is the key to design efficient numerical algorithms that make full use of the evanescent waves at hand.

On the other hand, when multiple frequency data is available, one theoretically challenging problem is to investigate the stability for the inverse scattering problem. It is believed that a Hölder type stability estimate can be obtained with sufficiently large band of frequencies.

# BIBLIOGRAPHY

# BIBLIOGRAPHY

- [1] E. Abbe, *Beiträge zur Theorie des Mikroskops und der mikroskopischen-Wahrnehmung*, Archivf. Mirooskop. Anat., **9**, (1873), 413.
- [2] M. Abramowitz and I. Stegun (Eds.), *Handbook of Mathematical Functions with Formulas, Graphs, and Mathematical Tables*, NBS Applied Mathematics Series 55, National Bureau of Standards, Washington, DC (1964).
- [3] H. Ammari, G. Bao, and A.W. Wood, *An integral equation method for the electromagnetic scattering from cavities*, Math. Meth. Appl. Sci. **23** (2000), 1057-1072.
- [4] H. Ammari, G. Bao, and A.W. Wood, *Analysis of the electromagnetic scattering from a cavity*, Japan J. Indust. Appl. Math. **19** (2002), 301-310.
- [5] K. Belkebir, P. Chaumet, and A. Sentenac, *Superresolution in total internal reflection tomography*, J. Opt. Soc. Am. A, **22** (2005), 1889-1897.
- [6] K. Belkebir and A. Sentenac, *High-resolution optical diffraction microscopy*, J. Opt. Soc. Am. A, **20** (2003), 1223-1229.
- [7] G. Bao and P. Li, *Inverse medium scattering for three-dimensional time harmonic Maxwell equations*, Inverse Problems, **20** (2004), L1-L7.
- [8] G. Bao and P. Li, *Inverse medium scattering problems for electromagnetic waves*, SIAM J. Appl. Math., **65** (2005), 2049-2066.
- [9] G. Bao and P. Li, *Inverse medium scattering problems in near-field optics*, J. Comput. Math., **25** (2007), 252-265.
- [10] G. Bao and J. Lin, *Near-field imaging of the surface displacement on an infinite ground plane*, submitted.
- [11] G. Bao and J. Lin, *Imaging of local surface displacement on an infinite ground plane: the multiple frequency case*, submitted.

- [12] G. Bao, J. Lin, and F. Triki, *A multi-frequency inverse source problem*, J. Differential Equations, **249** (2010), 3443-3465.
- [13] G. Bao and F. Triki, *Error estimates for the recursive linearization for solving inverse medium problems*, J. Comput. Math., **28** (2010), 725-744.
- [14] J. Baumeister, *Stable Solutions of Inverse Problems*, Vieweg-Verlag, Braunschweig, (1987).
- [15] M. Bertero, P. Boccacci and M. Piana, *Resolution and super-resolution in inverse diffraction*, Lecture Notes in Physics **486** (1997), 1-17.
- [16] H. Bialy, *Iterative Behandlung linearer Funktionalgleichungen*, Arch. Rat. Mech. Anal. **4** (1959), 166.
- [17] M. Born and E. Wolf, *Principles of Optics* (6th ed.), Cambridge Univ. Press, 1980.
- [18] R. Carminati and J. Greffet, *Influence of dielectric contrast and topography on the near field scattered by an inhomogeneous surface*, J. Opt. Soc. Am. A, **12** (1995), 2716-2725.
- [19] P. Carney and J. Schotland, *Inverse scattering for near-field microscopy*, Appl. Phys. Lett. **77** (2000), 2798-800.
- [20] P. Carney and J. Schotland, *Three-dimensional total internal reflection microscopy*, Opt. Lett. **26** (2001), 1072-1074.
- [21] P. Chaumet, K. Belkebir, and A. Sentenac, *Numerical study of grating-assisted optical diffraction tomography*, Phy. Rev. A, **76** (2007), 013814.
- [22] Y. Chen, *Inverse scattering via Heisenberg's uncertainty principle*, Inverse Problems, **13** (1997), 1-13.
- [23] D. Colton and R. Kress, *Integral Equation Methods in Scattering Theory*, Pure and Applied Mathematics, Wiley, New York (1983).
- [24] D. Colton and R. Kress, *Inverse Acoustic and Electromagnetic Scattering Theory*, Applied Mathematical Sciences, Vol. 93, Springer-Verlag, Berlin (1998).
- [25] D. Courjon and C. Bainier, *Near field microscopy and near field optics*, Rep. Prog. Phys. **57** (1994), 989-1028.
- [26] D. Courjon, K. Sarayeddine, and M. Spajer, *Scanning tunneling optical microscopy*, Opt. Commun. **71** (1989), 23-28.
- [27] J. W. Daniel, *The conjugate gradient method for linear and nonlinear operator equations*, SIAM J. Numer. Anal. **4** (1967), 10-26.

- [28] C. de Boor, *A Practical Guide to Splines*, Applied Mathematical Sciences, vol. 27, Springer-Verlag, New York (2001).
- [29] G. Derveaux, G. Papanicolaou and C. Tsogka, *Resolution and denoising in near-field imaging*, *Inverse Problems* **22** (2006), 1437-1456.
- [30] R. Dunn, *Near-Field Scanning Optical Microscopy*, *Chem. Rev.* **99** (1999), 2891-2927.
- [31] H. W. Engl, M. Hanke, and A. Neubauer, *Regularization of Inverse Problems*, Mathematics and Its Application, Kluwer Academic Publishers, New York (1996).
- [32] H. W. Engl, K. Kunisch, and A. Neubauer, *Convergence rates for Tikhonov Regularization of nonlinear ill-posed problems*, *Inverse Problems*, **5** (1989) 541-547.
- [33] B. Engquist and A. Majda, *Absorbing boundary conditions for the numerical simulation of waves*, *Math. Comput.*, **31** (1977), 629-651.
- [34] L. C. Evans, *Partial Differential Equations*, Graduate Studies in Mathematics, Vol. 19, American Mathematical Society (1997).
- [35] V. Fridman, *A method of successive approximations for Fredholm integral equations of the first kind*, *Uspekhi Mat. Nauk.*, **11** (1956), 233-234.
- [36] J. Graves and P. M. Prenter, *Numerical iterative filters applied to first Fredholm integral equations*, *Numer. Math.*, **30** (1978), 281-299.
- [37] C. W. Groetsch, *The Theory of Tikhonov Regularization for Fredholm Equations of the First Kind*. Pitman, Boston (1984).
- [38] J. Hadamard, *Lectures on Cauchy's problem in Linear Partial Differential Equations*, Yale University Press, New Haven (1923).
- [39] M. Hanke, A. Neubauer, and O. Scherzer *A convergence analysis of the Landweber iteration for nonlinear ill-posed problems*, *Numer. Math.*, **72** (1995), 21-37.
- [40] V. Isakov, *Increasing stability for the Schrödinger potential from the Dirichlet-to-Neumann map*, *Discrete Contin. Dynam. Systems-S*, to appear.
- [41] D. Jerison and C. Kenig, *Unique continuation and absence of positive eigenvalues for Schrödinger operators*. *Ann. Math.*, **121**(1985), 463-488.
- [42] J. Jin, *The Finite Element Method in Electromagnetics (2nd ed.)*, John Wiley & Sons (2002).
- [43] A. Kirsch, *An Introduction to the Mathematical Theory of Inverse Problems*, Applied Mathematical Sciences, Vol. 120, Springer-Verlag, New York, 1996.

- [44] A. Kirsch, *The domain derivative and two applications in inverse scattering theory*, Inverse Problems, **16** (1993), 81-96.
- [45] R. Kress, *Linear Integral Equations*, Applied Mathematical Sciences, Vol. 82, Sringer-verlag, New York (1999).
- [46] R. Kress and T. Tran, *Inverse scattering for a locally perturbed half-plane*, Inverse Problems **16** (2000), 1541-1559.
- [47] D. Labeke and D. Barchiesi, *Scanning-tunneling optical microscopy: a theoretical macroscopic approach*, J. Opt. Soc. Am. A **9** (1992), 732-739.
- [48] L. Landweber, *An iteration formula for Fredholm integral equations of the first kind*, Am. J. Math. **73** (1951), 615-624.
- [49] V. A. Morozov, *On the solution of functional equations by the method of regularization*, Soviet Math. Dokl **7** (1966), 414-417.
- [50] A. Neubauer, *Tikhonov Regularization for nonlinear ill-posed problems: optimal convergence and finite-dimensional approximation*, Inverse Problems, **5** (1989) 541-547.
- [51] L. Novotny and B. Hecht, *Principles of Nano-Optics*, Cambridge University Press (2006).
- [52] O. Pironneau, *Optimal Shape Design for Elliptic Systems*, Springer-Verlag, New York (1984).
- [53] L. Rayleigh, *On the theory of optical images with special reference to the optical microscope*, Phil. Mag. **5** (1896), 167-195.
- [54] R. C. Reddick, R. J Warmack, D. W. Chilcott, S. L. Sharp , and T. L. Ferrel, *Photon scanning tunneling microscopy*, Rev. Sci. Instrum. **61** (1990) 3669-3677.
- [55] T. I. Seidman and C. R. Vogel, *Well-posedness and convergence of some regularization methods for nonlinear ill-posed problems*, Inverse Problems, **5** (1989) 227-238.
- [56] J. Sokolowski and J. Zolesio, *Introduction to Shape Optimization: Shape Sensitivity Analysis*, Springer-Verlag, Berlin (1992).
- [57] J. Sun, P. Carney, and J. Schotland, *Near-field scanning optical tomography: a nondestructive method for three-dimensional nanoscale imaging*, IEEE J. Sel. Top. Quant. **12** (2006), 1072-1082.
- [58] S. Twomey, *The application of numerical filtering to the solution of integral equations encountered in indirect sensing measurements*, J. Franklin Inst. **279** (1965), 95-109.

- [59] A. V. Tikhonov, *On the solution of incorrectly formulated problems and the regularization method*, Soviet Math. Doklady, **4** (1963), 1035-1038.
- [60] A. V. Tikhonov, *Regularization of incorrectly posed problems*, Soviet Math. Doklady, **4** (1963), 1624-1627.
- [61] A. Willers, *The Helmholtz equation in disturbed half-spaces*, Math. Meth. Appl. Sci. **9** (1987), 312-323.
- [62] E. Wolf (Ed.) *Progress in Optics* **50**, Elsevier, Amsterdam, The Netherlands (2007).
- [63] A. Wood, *Analysis of electromagnetic scattering from an overfilled cavity in the ground plane*, J. Comput. Phys., **215** (2006), 630-641.
- [64] B. Zhang and S. N. Chandler-Wilde, *Integral equation methods for scattering by infinite rough surfaces*, Math. Meth. Appl. Sci. **26** (2003), 463-488.